EFFECTS OF MANUFACTURING PROCESS VARIABLES ON ULTRASONIC TESTING IN ELECTRON BEAM MELTED TI-6AL-4V

THESIS

Andrew D. Durkee, Captain, USAF

AFIT-ENY-MS-18-M-254

DEPARTMENT OF THE AIR FORCE
AIR UNIVERSITY

AIR FORCE INSTITUTE OF TECHNOLOGY

Wright-Patterson Air Force Base, Ohio

AFIT-ENY-MS-18-M-254

EFFECTS OF MANUFACTURING PROCESS VARIABLES ON ULTRASONIC TESTING IN ELECTRON BEAM MELTED TI-6AL-4V

THESIS

Presented to the Faculty

Department of Aeronautical Engineering

Graduate School of Engineering and Management

Air Force Institute of Technology

Air University

Air Education and Training Command

in Partial Fulfillment of the Requirements for the

Degree of Master of Science in Aeronautical Engineering

Andrew D. Durkee, B.S.M.E.

Captain, USAF

March 8, 2018

AFIT-ENY-MS-18-M-254

EFFECTS OF MANUFACTURING PROCESS VARIABLES ON ULTRASONIC TESTING IN ELECTRON BEAM MELTED TI-6AL-4V

Andrew D. Durkee, B.S.M.E.
Captain, USAF

Committee Membership:

Andrew J. Lingenfelter, PhD
Chair

David Liu, PhD
Member

Edwin Schwalbach, PhD
Member

Marc Polanka, PhD
Member

Abstract

Further research on validating Additive Manufacturing production quality is required before the realization of direct print-to-fly application of critical components. Non-Destructive Inspection shows promise as a valuable tool for part validation. Understanding techniques for accurate natural flaw replication through intentional void modeling and treatment is crucial to assessing Non-Destructive Inspection methods for real-world applications. This research examines the response of Ultrasonic Testing as a function of various manufacturing variables in Electron Beam Melted samples of Ti-6Al-4V. Four dimensionally identical blocks with 6 spherical, 1 mm voids at varying depths were manufactured using different combinations of stock powder, edge treatments, and void melting. Ultrasonic Testing scans were completed on two sides of each specimen with the transducer focused on the mid-plane. Additionally, one specimen was scanned six times, with the focal plane adjusted for each scan to match the depth of each void. Image processing techniques were then used to analyze each scan. Scans completed along the build layers with all voids in plane with the transducer's focus identified the most voids. Scans through the build layers with voids at varying distances from the transducer focus were more difficult to identify and most were indistinguishable from other signal returns. However, the use of back wall returns increased the probability of detection. Overall, powder selection had the greatest influence on image quality and detection success, while contour and melting modes have significantly lower effects.

Acknowledgments

I would like to extend my sincere gratitude to my research advisors, Capt Andrew Lingenfelter and Maj David Liu for their guidance and encouragement throughout this thesis effort. I would also like to thank Dr. Edwin Schwalbach Mr. Norman Schell and Mr. Josiah Dierken of the Air Force Research Laboratories, Materials and Manufacturing Directorate, for their endless support, knowledge, and assistance throughout this project. Additionally I want to thank my sponsor, Mr. Dennis Lindell and the Joint Aircraft Survivability Program.

Andrew D. Durkee

Contents

Page

List of Figures

List of Tables

EFFECTS OF MANUFACTURING PROCESS VARIABLES ON ULTRASONIC TESTING IN ELECTRON BEAM MELTED TI-6AL-4V

I. Introduction

1.1 Background

Additive Manufacturing (AM) is a class of manufacturing technology that produces near-net shape products, where the initial shape of a manufactured item closely resembles its final form. The first applications of AM was in the production of small-batch samples and prototypes, but has grown into a full-scale fabrication capability. AM provides these capabilities with reduced cost and production time and virtually no waste [1]. Additionally, specialized tooling is not required and the simultaneous manufacture of unique, separate parts is possible. This allows the use of smaller single machines to produce larger parts, replacing entire production facilities with several AM machines.

With its extensive potential as a new manufacturing method, the aerospace industry is seeking to integrate AM into existing production methods, either through the rapid fabrication of unique prototypes, or through the use of full-scale AM production facilities [2]. Industrial application of AM is expected to grow as part quality and materials improve. Additionally, AM allows the design of complex optimized parts which are impossible to manufacture with traditional manufacturing technologies [3]. No longer limited to today's manufacturing technology, this would allow the design of lighter, yet stronger aircraft components, reducing fuel consumption and overall operating costs [4].

1.2 Motivation for Research

Within the aerospace industry, the advancement of AM technologies has the potential to transform the manufacturing flexibility of small and remote facilities, such as those in flight line level units or in deployed locations. This would allow the on-site manufacture of components, as needed, alleviating part demand and supply line strain. This "print-to-fly" capability of AM especially apply to aircraft battle damage repair (ABDR), where combat damage may require the replacement of critical aircraft components not typically kept on hand, or in the case of an aging aircraft fleet, not currently in production.

Before the realization of "print-to-fly" capability of AM, potential users must master several unique factors of the technology. While AM produces near-net shape components, many parts used in the aerospace industry require much tighter tolerances than current AM methods can produce. Additionally, in order to function properly, the contact points of moving parts require smooth surface finishes beyond the capabilities of current AM technologies. The use of post production machining can alleviate both of these issues, but would require additional equipment, time, and cost to produce a component [3].

Lastly, since the technology is additive by nature, AM can generate unintentional defects such as voids, gaps, or flaws during the manufacturing process itself. These defects are detrimental to strength and fatigue life of critical components. Currently, two methods are being researched in the industry to limit the effect of this issue. The first is the use of monitoring systems during the manufacture of parts to detect and potentially correct a flaw as it occurs [5]. The biggest challenge to this technique is the requirement to constantly monitor a part during manufacture. The second is to use Non-destructive Inspection (NDI) techniques to inspect parts after completion for vacancies detrimental to the component's use [6].

1.3 Problem Statement

While UT is a low-cost, low lead-time NDI method, there is currently no specific methodology or technique for its use on AM metal components. Current Air Force Research Laboratory (AFRL) efforts in AM seek to qualify the use of NDI techniques for use in post-fabrication inspection of production-representative parts. However, in order to properly qualify these techniques, further research is required to determine how the manufacturing of intentional voids in test specimens effects the results of NDI. This research seeks to assess what effects various manufacturing treatments have on UT scanning when used to detect known voids in a test specimen.

1.4 Research Scope

The purpose of this research is to investigate the use of ultrasonic testing (UT) on Electron Beam Melting (EBM) Ti-6Al-4V. In order to realize the print-to-fly capability potential of AM technologies, NDI on fatigue-critical components is required before their installation [6]. Additional data on void manufacture treatments will develop a greater understanding of inspection techniques on defect detection test specimens. The focus of the research conducted in this study to investigate the impact of manufacturing process variables on UT response in EBM Ti-6Al-4V. The specimens tested in this thesis are representative of an array of potential methods for manufacturing voids for testing NDI techniques.

1.5 Research Objectives

The goal of this research is to assess the response of UT when used to detect known voids in EBM Ti-6Al-4V alloy when fabricated with various manufacturing

treatments. To assess these manufacturing treatments or process variables, this research will focus on the following objectives:

1. Determine the influence of different source powder, contour modes and melting modes on UT results.

2. Determine the influence of varying distances from transducer focal plane on UT results.

3. Determine the influence of build direction relative to scan direction on UT results.

To complete these objectives, data was collected from four samples in two configurations. All samples were manufactured by Oak Ridge National Laboratories on an Arcam Model A2 EBM machine.

1.6 Assumptions and Limitations

The research in this thesis contains experimental data collected from four EBM Ti-6Al-4V specimens using a computer controlled UT scanner in a submersion tank. This data is limited to the extent of the manufacturing and material quality at the time of their fabrication. It is assumed the voids were manufactured as designed and closely match the design specifications. Due to time, resource, and equipment limitations, all specimens have fixed void dimensions and locations. Additionally, fabrication of the specimens was completed before the scope of this research was defined. All manufacturing conditions were determined at the time of fabrication and manufacturing variables other than those investigated are not within the scope of this research.

1.7 Chapter Outline

This chapter presented a brief background and overview of the proposed research objectives for this thesis. A review of current literature and a more thorough discussion of the theory and technologies utilized in this research is presented in Chapter Two. Chapter Three will present the procedures followed to collect and analyze data and Chapter Four will present the results of this analysis. This thesis will conclude with Chapter Five, which will discuss the results presented as well as future work.

II. Background & Theory

2.1 Additive Manufacturing

Additive Manufacturing (AM), colloquially referred to as "3-D Printing," is a three-dimensional manufacturing method using a layer-by-layer build-up process [7]. Unlike traditional manufacturing methods such as machining, cutting, molding, or casting processes, AM builds a component in layers from a raw stock material. AM components are typically built from computer-generated files allowing the production of complex geometries without complicated tooling. The production of metal components is achieved through several AM techniques, including: Direct Metal Laser Sintering (DMLS), Direct Metal Deposition (DMD), Electron Beam Free Form Fabrication (EBF3) and Electron Beam Melting (EBM) [7]. This report will primarily focus on EBM AM.

AM was first developed in 1986 with a technique known as Stereolithography Rapid Printing Systems. These machines used a movable ultraviolet laser that cured layers of photo-sensitive liquid acrylate. This technology quickly spread as it allowed the easy and cost-effective production of three dimensional prototypes and models. This allowed designers and engineers in many industries to design, test-fit, and tweak parts before they were produced in more robust, and expensive, manufacturing methods [1].

With the growing popularity of polymer AM processes, adapting the growing technology to metal components was the next logical step. Powder Bed Fusion (PBF) was the first and most successful category of metal AM techniques developed [7]. Within PBF, there are four primary techniques used to fuse the powdered build layer into a complex shape: full melting, liquid-phase sintering, solid-state sintering, and chemically-induced binding. Full melting is achieved through the application of

directed energy to heat the powder to a molten state, fusing the powder for each layer of a part. In liquid-phase sintering, only a portion of the powder particles are elevated to molten temperatures, fusing with surrounding solid powder particles. Solid-state sintering fuses powder at temperature levels below molten temperatures. Chemically-induced sintering is based on the use of chemically reactive powders to bond a layer together. Chemically-induced sintering has allowed the usage of structural ceramics, since ceramic materials typically have a melting temperature that is too high for other PBF AM techniques.

AM machines using PBF start with a powder of the desired material stored in hoppers. A thin layer of the powder is then spread using a rake or blade across the build layer. A directed energy source, such as a laser in SLS, or an electron beam in EBM, is then used to fuse the powder together based on the programming in the governing computer model. Once the layer is complete, the build plate is lowered and another layer of powder is spread. The unmelted powder remains in place as a means of support. This process is then repeated until a completed component is produced. Excess powder is then removed and the part is detached from the build plate, typically via wire electrical discharge machining (EDM) [8].

2.2 Electron Beam Melting

Electron Beam Melting (EBM) is a form of PBF AM that utilizes a focused electron beam to fuse layers of powdered material into a three dimensional shape. Originally developed by Arcam in 1997, EBM produces dense parts from engineering alloys in an atmospherically sealed, fully automated system. The build chamber is preheated and held in vacuum, which reduces residual stresses and provides a non-oxidizing environment to ensure material purity throughout the component [9].

EBM systems consist of three primary components: an electron beam generator, the build chamber, and a computer controller. The electron beam generator is composed of an electron gun, where a high current is passed through a tungsten filament which produces an electron beam. This electron beam is then shaped and directed by a series of electromagnetic lenses. The build chamber surrounds a movable build plate, powder hoppers and a rake mechanism to deposit each layer of the build material. The computer controller accepts outside inputs and controls the entire process throughout the manufacture of a component. Figure 2.1 shows a schematic of a typical EBM system.

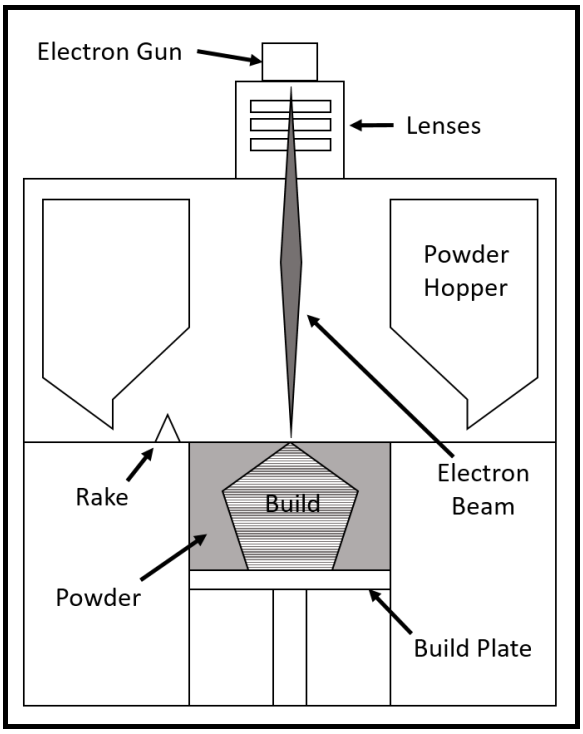

Figure 2.1. Schematic of a typical Electron Beam Melting Machine.

Similar to most AM processes, the manufacture of a part starts with a digital computer aided design (CAD) model. This model is then virtually sliced into layers and fed into the EBM system, which reproduces the slices in the build chamber, layer by layer. Once a layer is completed, the build plate is lowered by the required layer

thickness. The rake then deposits a thin layer of powder from one of two hoppers. Preheating is required by use of the electron beam. The addition of heat sinters the powder bed, which reduces the build up of electric charge that would result in coulomb repulsion between particles. Depending on the material used, the build plate material will differ in thermal properties to ensure ease of removal of the completed component [9].

EBM differs from other PBF techniques in a number of ways. As previously discussed, EBM systems operate in a vacuum, as opposed to most PBF systems, whose build chambers are typically filled with an inert gas. Additionally, the electron beam is used to preheat the build chamber, where other PBF systems require additional heating equipment for this process. The use of thermal cameras monitoring cameras and FEA simulation has increased the efficiency of this benefit, allowing accurate modeling and monitoring of heat build up within the part during manufacture [10]. Lastly, EBM is able to steer the energy source quicker since the electron beam is controlled by electromagnetic lenses, whereas other PBF systems, such as SLS, rely on mechanical mirrors and optical lenses. This, combined with the use of coarser powders and thicker components results in faster build times [7].

2.3 Titanium Alloy, 6% Aluminum, 4% Vanadium

Often used in high performance structures, titanium alloys are lightweight, high strength metal alloys that offer high corrosion resistance, low coefficient of thermal expansion and high fracture toughness, especially at temperatures up to 400°Celsius. These material properties are controlled through alloying and heat treatment. Titanium alloys are separated into two categories: alpha and beta phase alloys. Alpha alloys behave similarly to raw titanium and are not typically heat treatable. While they have lower strength overall, alpha alloys are stronger at extremely low tem-

peratures, have increased ductility and accept welds readily. Beta alloys are more heat treatable and stronger, especially at higher temperatures, but have lower ductility and are more difficult to weld. While titanium alloys have very high specific strength, especially in high heat applications, these features come at significant material and manufacturing cost over common materials such as steels or aluminum alloys. Despite this cost, they see frequent use in aerospace, biomedical and other high-end structural applications [11].

Titanium alloy, 6% aluminum, 4% vanadium (Ti-6Al-4V), is an alpha-beta titanium alloy, meaning that it contains both alpha and beta phases at room temperature [12]. The alpha phase behaves similarly to unalloyed titanium but is strengthened through the addition of aluminum. The beta phase component is stabilized with vanadium, providing the high temperature characteristics of titanium at room temperature. This alloy is one of the most commonly available alloys of titanium and its powdered form used in the EBM process is the primary material of focus in this research [11].

2.4 Nondestructive Inspection

Non-destructive Inspection (NDI), is the application of several techniques to detect flaws or defects within a component without requiring direct observation of the component's interior. The end goal of NDI is to verify and validate the structural function of a specific part without preventing its future use. This is especially vital in the maintenance of critical aerospace components where defects can lead to critical weakening and eventual failure. Depending on the method used, NDI can detect the presence of a flaw as well as additional information such as location, size, and shape.

Due to its extensive fleet of aerospace systems, the United States Air Force (USAF) invests heavily in NDI research and applications [13]. The USAF classifies five stan-

dard types of NDI: Liquid Penetrant, Magnetic Particle, Eddy Current, Radiography, and Ultrasonic [14]. Ultrasonic inspection is the primary NDI method used in this research. NDI methods compile an accurate way to detect flaws when operated by a well-trained technician, providing maintenance personnel and program engineers tools to determine serviceability of critical components before ultimate fatigue or failure can occur.

During component acquisitions, six stages of inspection are used to validate and verify new aircraft components: first article inspection, receiving inspection, manufacturing and assembly inspection, data gathering, vendor qualification, and capability demonstration. First article inspection verifies that a manufacturer meets or exceeds the part specifications before delivery. Receiving inspections are completed on incoming components to ensure quality. Manufacturing and assembly inspections are completed on raw stock prior to a manufacturing process that would preclude future inspection, and to ensure material quality. Vendor qualification is completed as an audit process of component and material suppliers.

NDI is especially critical in AM components as the manufacture process is more susceptible to flaws and defects [15]. Additionally, machine to machine repeatability remains a concern for part consistency as well as final qualification and certification. However, several unique aspects of AM components require further research before NDI is accurately and reliably integrated into AM protocols. These research areas include: complex part geometry, rough surface finishes, variable and complex grain structure, and undefined critical defect types, sizes and shapes [6].

2.5 Ultrasonic Inspection

Ultrasonic inspection is an NDI technique that uses high-frequency mechanical waves to detect discontinuities in a solid or liquid medium [16]. The use of ultra-

sonic waves allows penetrating internal inspection capabilities not provided by other forms of NDI. Additionally, since ultrasonic waves do not require a magnetically or electrically conductive material, UT is also one of the most flexible forms of NDI and is used on various structural materials including carbon fiber composites and titanium alloys. Due to this combination of penetration power and flexibility, UT can detect a number of variables or properties in a target material, including: flaws, voids, inclusions, disbond, material thickness and density [16].

In UT transducers, high-frequency mechanical waves are generated by transforming electrical energy into mechanical waves using a piezoelectric element [16]. The frequency produced by a transducer is determined by the material and size of this piezoelectric element. This element is also capable of detecting ultrasonic energy and transforming it back into electrical energy. Due to the high and variable acoustic impedance of air, a coupling material is typically used to ensure consistent energy transmittance between the transducer and the test specimen [16].

As an ultrasonic wave is transmitted through a sample material, several types of interactions can occur, including: diffraction, scattering, absorption, reflection, and refraction [16]. Reflection is the most important factor investigated for this research. When a wave propagates through a material to an area of discontinuity, the interactions between atoms can change. This change leads to a portion of the energy wave dispersing with some of the wave being reflected directly back to the transducer. The transducer captures this reflection as a change in the energy return, measured by the piezoelectric element.

Transducers used in UT produce two types of beams, focused and unfocused [16]. Unfocused beams allow the acoustic energy from the transducer to spread out. While an unfocused beam has a greater chance of detecting discontinuities near to the surface of a sample, energy is dissipated quickly, which can cause issues when used on thicker

samples. A focused beam uses an acoustic lens to focus the ultrasonic beam from the transducer, providing a higher resolution scan. This increased resolution occurs when the beam is focused at or near an area of interest and therefore requires knowledge of the flaw under inspection in order to provide the best result [16].

As a transducer emits ultrasonic waves, it is also receiving reflected energy between each pulse. These reflections are displayed on an oscilloscope as an amplitude of the received energy as a function of time [16]. A mechanical wave's velocity in a homogeneous medium, V_L, can be assumed to be constant and is governed by the mechanical properties: modulus of elasticity (E), Poisson's ratio (ν), and density (ρ). For an isotropic material of sufficient thickness, V_L can be estimated using Equation 2.1, below [16].

$$V_L = \sqrt{\frac{E(1-\nu)}{\rho(1+\nu)(1-2\nu)}} \tag{2.1}$$

Since V_L is constant for a given material, the time between the signal and its return is directly proportional to the distance the wave traveled. This data is referred to as an A-Scan, shown in Figure 2.2. When a UT transducer is mounted in a computer controlled arm, multiple A-scans can be collected along a precisely controlled path. By measuring multiple points in a sample, several A-scans are typically combined into a C-scan, shown in Figure 2.3. To generate a C-scan, the maximum amplitude in each A-scan collected is assigned a value between 0 and 255, where 0 corresponds to zero amplitude and 255 corresponds to the maximum amplitude observed among all A-scans. Each A-scan value is then coordinated with a pixel in a greyscale image providing a planar view of the specimen.

Once an A-scan from a handheld UT device or a C-scan from a computer controlled UT system is produced, a UT technician will analyze the results to determine the presence of a flaw [16]. A technician is trained to search for sudden changes in

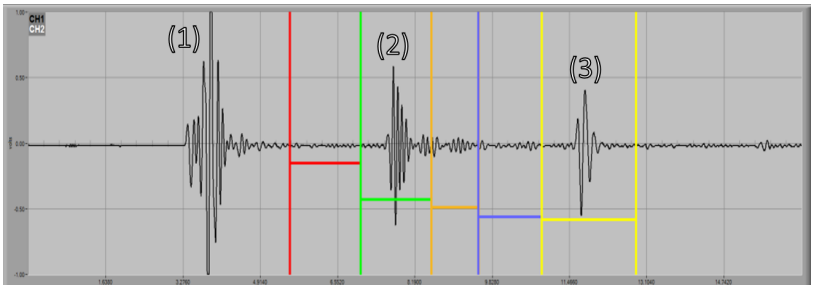

Figure 2.2. Example A-scan as viewed on Digital Oscilloscope. In this A-scan, several clear returns are seen, including: (1) the front wall return, (2) a void, and (3) the back wall return.

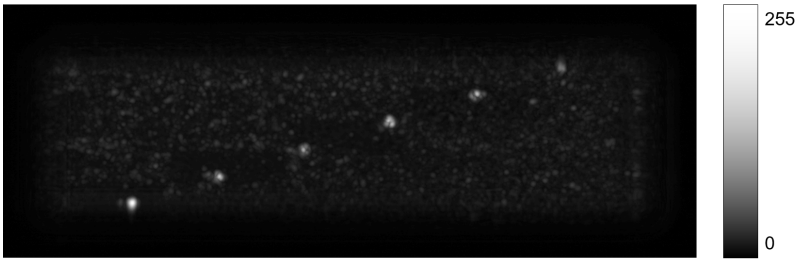

Figure 2.3. Example C-scan generated from multiple A-scans. Maximum amplitude returns are assigned a pixel value, with higher pixels indicating stronger returns. Six voids are shown in this C-scan

return amplitudes and while voids and flaws are often readily detectable by human operators in large homogeneous structures, this process is quite subjective and relies on the quality of a technicians training and experience.

2.6 Greyscale Image Processing

Due to the complex and often subjective nature of UT scan analysis, digitally automated methods are sought to replace manual inspection of UT imagery [17]. As discussed in the previous section, C-scans provide a great deal of information. However, this quantity of data presents difficulties when deciphering and results in subjectivity when unclear data is presented to a human operator. Using automated computer algorithms to detect flaws or defects from an inputted C-scan image can provide faster, cheaper and potentially more consistent results than relying on a

human technician. Additionally, computerized analysis can provide objective analysis when attempting to qualify NDI technologies for use on new manufacturing methods such as AM.

In an attempt to achieve automated analysis of UT scans, researchers at TNO Industry developed a technique that used a reference image for comparison [17]. Using a sample specimen with a known geometry, the researchers built a reference image using computer models and a morphological filter. Test specimens were then manufactured with intentional defects in known locations and scanned using UT. After completing UT scans on the test specimens, this reference image was then compared with collected C-scans to determine defect locations. Using this technique, all known voids were detected. However, a large number of false positives were also identified. While this technique is promising, reducing the high number of false positives is critical before application of such a technique is applied to a production line.

2.6.1 Circular Hough Transform

This research identified two image processing techniques that can automatically identifying unique image features in UT C-scan images. The first technique studied is the Circular Hough Transform. The Hough Transform is a feature extraction technique used to detect circular objects in a digital image [18]. The transform searches for unique pixels in a search space and generates a 3-dimensional parameter space (a, b, r) for that pixel based on the equation for a circle in Equation 2.2, where a and b are the coordinates of the center of the circle, and r is the radius.

$$(x - a^2) + (y - b^2) = r^2 \tag{2.2}$$

This parameter space is then compared with other spaces for other pixels and an accumulator matrix is developed from intersections of parameter spaces. An algorithm

is then used to "vote" for the most likely inputs to a circular form factor based on the accumulator matrix. The resulting points are set as the circumference of a circle. These points are identified and collected, with location and radius data. An example of this process is shown in Figure 2.4, below.

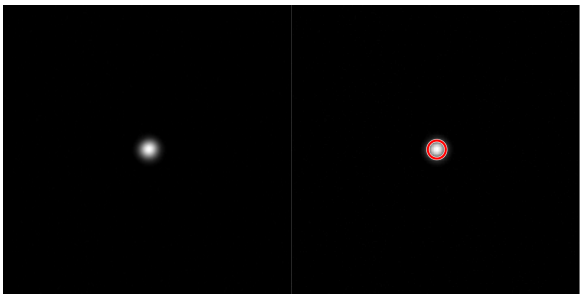

(a) **(b)**

Figure 2.4. Example circular hough transform performed on UT C-scan of a #2 Flat Bottom Hole Standard

2.6.2 Speeded Up Robust Features

The second image processing technique investigated was Speeded Up Robust Features (SURF). SURF is a scale invariant processing technique designed to detect and describe unique features in a digital image using local pixel gradients [19]. Developed from a method known as Scale-Invariant Feature Transform, SURF is reported as a faster, more robust and less resource intensive image processing technique. Using integral images, a 6-pixel grid filter is used to approximate Gaussian blurring. From these grids, integral approximations of Hessian matrices are developed.

The Hessian Matrix is a multivariable matrix of all partial derivatives of the pixel gradient at a point. SURF then calculates the vertical and horizontal wavelet responses from these matrices and identifies points of interest. In addition to location, the SURF processing function outputs interest point direction, and a strength metric. The dominant direction is calculated by a voting algorithm that uses the sum of all wavelet responses in a sliding 60 degree window. While useful in detection and

tracking algorithms used in video, direction is often not useful and ignored in static 2-dimensional images [19]. An example of this process performed on a UT C-scan can be seen in Figure 2.5, below.

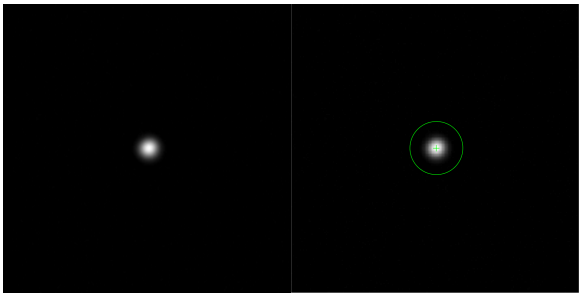

(a) **(b)**

Figure 2.5. Example SURF transform performed on UT C-scan of a #2 Flat Bottom Hole Standard

The strength metric is a unitless value calculated by taking the determinant of the Hessian Matrix at the point of interest [19]. Since the determinant is the sum of component products, this strength metric calculates the steepness of the pixel gradient in all directions. Since UT C-scans are static 2-dimensional images, location and strength are the only outputs of interest for use in scan analysis. The location of a SURF point would identify the location or edges of a void while the strength metric can quantify the pixel gradient at the location and in turn correlate to the contrast of a void with its surroundings.

2.7 Current Research

As discussed in previous sections, the use of NDI on AM is a vital area of research for many industries. The ability to accurately detect, identify and track defects in AM parts, both during manufacture and throughout a part's lifetime, is critical for widespread adoption. Many recent and ongoing studies investigate the integration of current and novel NDI techniques with ongoing advancements in AM capabilities.

One example of research integrating NDI into AM processes was a study conducted by researchers at Virginia Tech. In an effort to monitor manufacturing quality, researchers used electronic impedance piezoceramic sensors to monitor the production of a polymer structure on a jetting AM system [20]. The sensors were used to verify the component was fabricated within tolerances, with no undesired voids or gaps. These voids or gaps would appear as a diversion of the electronic impedance of the component from a known baseline.

The integration of UT into the AM process has also been investigated. One study attempted to implement an onboard UT system to characterize a SLM process [21]. For testing, an ultrasonic probe was temporarily mounted the underside of the build platform on an SLM machine. During the manufacture of test samples with circular and semi-circular voids, the amplitude and time-of-flight of ultrasonic energy was recorded. Analysis of this data indicated a correlation between UT A-scans, laser power and build height. While the researchers concluded that such an online characterization system may provide indications to overall build quality, accurate detection and tracking of individual defects may not be possible.

Several studies researched the use of Laser Ultrasound (LU) as a NDI method for testing AM components. One such study used LU to search for defects within samples manufactured from powder and wire melted AM samples of INCONEL 718 and Ti-6Al-4V [22]. The LU scans indicated several voids that were then verified by X-ray computed tomography. Another study investigated the use of LU for identifying near surface (< 0.5 mm) defects [23]. For detection, b-scans were generated from LU data and compared with scans generated from "clean" AM and billet specimens. While the resulting b-scans indicated the presence of the seeded defects, the results were not as distinct as reference holes generated via electrical discharge machining (EDM). The authors concluded powder filled defects near the surface may not reflect the ul-

trasonic energy well enough compared to empty voids, and further process refinement is required. It was noted that both studies did not employ any automated detection techniques, and required substantial subjective interpretation of scan results.

In a study conducted in 2016, researchers used the circular hough transform to detect voids in UT scans [24]. For this research, several Ti-6Al-4V samples were manufactured via EBM to produce several rectangular prisms with intentional voids of varying size from 0.51 mm to 2.01 mm. All samples tested were fabricated using a gas atomized powder manufactured by Arcam. Each specimen was scanned using a computer controlled UT with 2.5, 5 and 10 MHz transducers. After producing C-scans from UT data, the circular hough transform was applied to the images in order to automatically detect the voids in the image. Also, due to the fact that the circular Hough transform provides a measured radius for the image feature, the researcher was able to roughly size each of the detected voids. Using a 10 MHz transducer, the researcher was able to successfully use the circular Hough transform to detect all voids, with both the as-manufactured and machined surfaces. It was also noted that all detected voids were of known location and the UT transducer focal plane was aligned with the voids. While the majority of the voids were successfully detected using this technique, the circular Hough transform applies only to circular voids and defects. Combined with high computing and memory requirements, the circular Hough transform has potentially limited use in production qualification NDI techniques.

III. Research Methodology

3.1 Chapter Overview

This chapter presents the methods used to determine Ultrasonic Testing (UT) effectiveness on Titanium alloy, 6% Aluminum, 4% Vanadium (Ti-6Al-4V) samples fabricated via Electron Beam Melting (EBM) with various manufacturing treatments. All test specimens used were previously designed by the Air Force Research Laboratories, Materials and Manufacturing Directorate (AFRL/RX) and manufactured by Oak Ridge Laboratories under the supervision of AFRL/RX engineers for the purpose of testing nondestructive inspection techniques. A portion of the methods used was previously presented [25].

3.2 Test Specimen Design

In order to test nondestructive inspection techniques, AFRL/RX designed 12 unique specimens manufactured with Ti-6Al-4V via EBM. Each specimen has a unique design feature representing the varying geometries of aerospace components, along with a number of intentional voids. A single control block was also designed with a constant geometry and no intended voids. Due to the build plate constraints of the EBM machine, each set of specimens was split into groups of six for manufacturing.

In order to focus the scope of this research, one design was chosen from the 12 designs. This design has a prismatic geometry of 91 mm long (X), 25 mm wide (Y), and 25 mm tall (Z). The design also contained six spherical voids with a diameter of 1 mm. Each void was evenly spaced along the longitudinal axis at varying depths of 2, 6.2, 10.4, 14.6, 18.8, and 23 mm. A schematic of this design is shown in Figure 3.1. The four specimens, shown in Figure 3.2, were built using differing treatment

techniques and designated RCN, RNN, PNN, and PNF. This naming convention identifies the powder: PREP (R) or P841 (P), contour mode: contour (C) or no contour (N), and melting mode: no melt (N) or focus change (F).

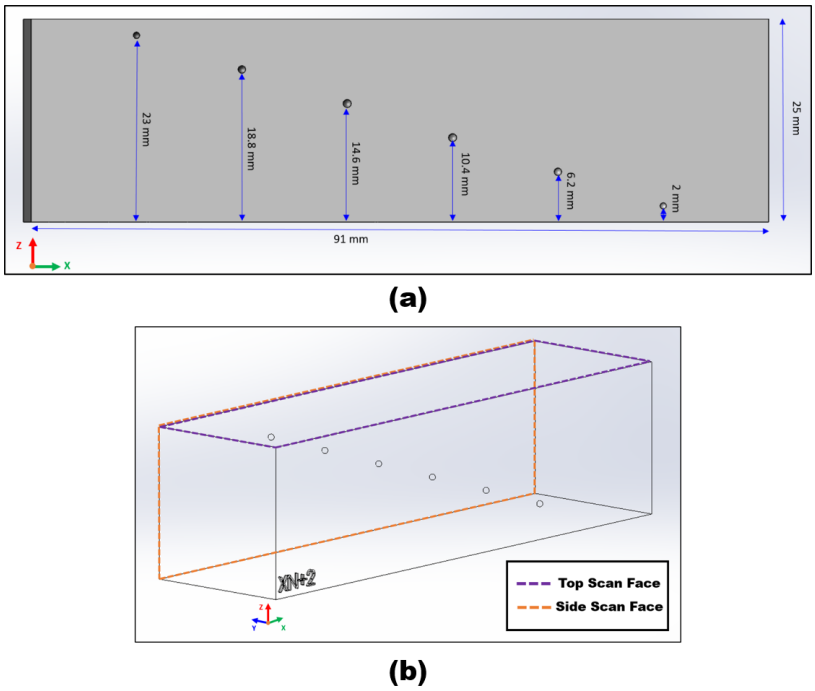

Figure 3.1. Cross Sectional Schematic of EBM Ti-6Al-4V Specimens. All specimens have the same dimensions, with the same manufactured voids. Each void is 1mm in diameter and evenly spaced along the X-axis in each build specimen. The machine finished top and side scan faces are identified in (b).

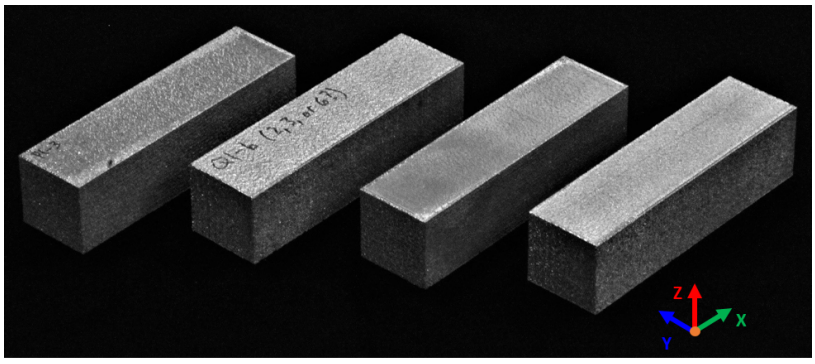

Figure 3.2. EBM Ti-6Al-4V Specimens. From left to right: RCN, RNN, PNN, and PNF blocks. All four samples are shown as manufactured, prior to surface finishing. Each block has a slightly different surface roughness due to the differing manufacturing treatments and powder stock used in production.

3.2.1 Orientation

To ensure a consistent reference frame for each specimen, a body-centric coordinate system was developed. A standard right-hand Cartesian coordinate axis was placed on the corner of each specimen such that the entire specimen is positioned in the postive-X, positive-Y, positive-Z quadrant. Using this reference frame, the voids are positioned with the highest void in the Z-axis closest to the origin and the lowest void in the Z-axis furthest from the origin, as shown in Figure 3.1. This reference frame also lines up with the vertical build direction of each specimen. During manufacturing, the first layer was started at Z=0 and was built vertically in the positive Z-direction. When completed, the XZ and YZ planes face the edges of the build layers while the XY plane lies parallel with the build layers. During fabrication, each block was rotated 10 degrees about the Z-axis to increase the fidelity of long edges during the EBM process. Due to this rotation, the reference frame used in this research is rotated 10 degrees from the original build plate axis of the EBM machine.

For UT processing, two faces on each specimen were also identified. These faces correspond to the XY plane at 25 mm and XZ plane at 25 mm. These planes are referred to as the top scan face, and side scan face, respectively, and are shown in Figure 3.1(b). When the top scan face is viewed, each void is equidistant from the X-axis but at varying depths. Additionally, the transducer will look through the build layers in this perspective. When the side scan face is viewed, each void is at varying distances from the X-axis. However, each void is at the same depth, approximately on the mid-plane. In this perspective, the transducer will look along the build layers.

3.3 Test Specimen Manufacturing

3.3.1 Specimen Fabrication

Each specimen was manufactured on separate productions at Oak Ridge Laboratories in Oak Ridge, Tennessee as a joint project with AFRL/RX. As mentioned in Section 3.2, test specimens were manufactured in groups of six in order to optimize manufacturing time. All specimens were built on an ARCAM A2 EBM machine. When designing the layout for the build plate, each design model was angled slightly offset to the machine's X-axis by 10 degrees. This angle was included to ensure the edges of each build were not parallel to the powder raking system. This minimized the disruption of powder distribution due the build up of component edges in the positive Z-direction. Figure 3.3 shows a frame taken from an infrared (IR) camera recording of the specimens during manufacture [26].

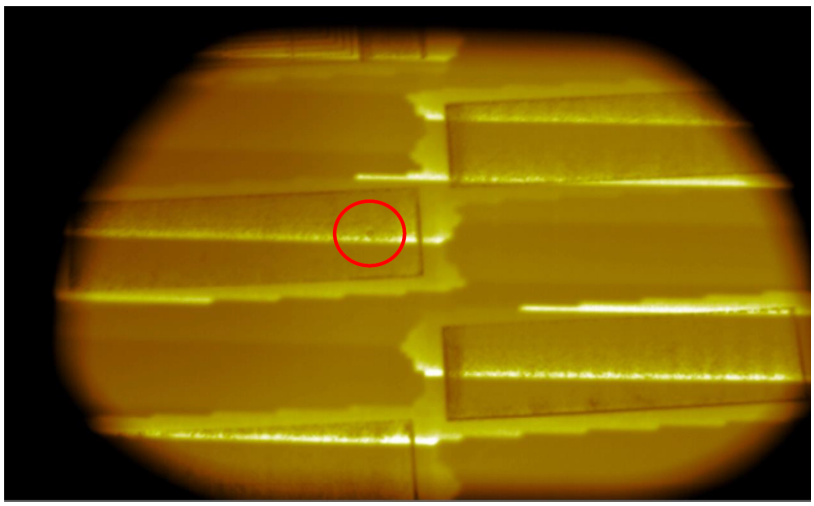

Figure 3.3. Infrared camera view of build plate during manufacturing of P1 specimens. Multiple passes of the electron beam are shown and are identified by bright horizontal lines. The built in angle of the specimens on the build plate are also shown. The red circle identifies the generation of a void [26].

3.3.2 Manufacturing Treatments

To observe the influence of the selected manufacturing variables on UT scan results, each production run utilized one of two different powder types, one of two different contour modes, and one of two defect modes. Table 3.1 identifies these factors for each of the specimens. The two different powder types used were referred to as Plasma Rotating Electrode Process (PREP) and Arcam P841 and atomized using differing techniques. PREP powder is manufactured through the use of a plasma heated solid bar of source material rotated inside a chamber. As the bar is rotated, molten droplets are centrifugally ejected, collected and then cooled to form spherical powder particles. Arcam P841 powder is a specific lot of wire atomized powder manufactured by Arcam. The creation of wire atomized powder consists of a wire spool simultaneously melted and cast off using a combination of plasma torches and gas jets.

The contour mode for each specimen specifies whether the edges of the manufactured voids were treated before the bulk of each build layer was melted. With contour mode activated, the EBM machine first traces the edges of the part profile with a more focused beam to ensure edge definition and better surface structural integrity. The beam then melts the powder bed layer within the part as defined by the computer aided design (CAD) drawing. With contour mode deactivated, this initial tracing step is skipped and the component edges receive the same energy focus and intensity as the rest of the build layer.

Table 3.1. Ti-6Al-4V Specimen Build Properties

Build Name	Powder Used	Contour Mode	Defect Mode
RCN	PREP	Yes	No Melt
RNN	PREP	No	No Melt
PNN	Arcam P841	No	No Melt
PNF	Arcam P841	No	Focus Change

Defect Mode dictates how the electron beam treats the internal voids of the specimen. In "No Melt" mode, the areas where the CAD drawing defines empty space receive no energy and the powder remains largely unmelted, with any powder cohesion resulting from conductive heat from the surrounding component. In "Focus Change" mode, after the initial melting pass, the electron beam passes over the areas of empty space and the EBM machine adjusts the electromagnetic lenses until the focal point of the electron beam is either above or below the build layer. In this mode, electron beam energy is still transmitted into the build powder. The energy absorbed in this area is less than received by the surrounding material, and the voids will contain only partially melted powder.

Previous research on EBM Ti-6Al-4V blocks indicated surface roughness has a significant impact on UT signal returns [24]. To minimize this effect, each specimen was processed to remove natural surface roughness. A shell end mill was used on a 3-axis mill to remove surface layers of each specimen until a relatively smooth finish was achieved. This surfacing treatment was the same used by Hanks and similar surface roughness results were achieved [24].

3.4 Ultrasonic Inspection of Test Specimens

Ultrasonic inspections were completed for each of the four specimens using AFRL's MaPPs II system. This system consists of a 3-axis controller, water immersion tank, pulse generator, and data acquisition system. A Panametrics 10 MHz, 12.7 mm focused beam transducer was used for all scans and had a water path focal length of 76.2 mm. In Ti-6Al-4V, this transducer produces a beam with a wavelength of 0.61 mm. Previous research on EBM Ti-6Al-4V found this transducer type produced the strongest response on voids approximately 1 mm in diameter [24]. Scans were collected through the thickness of each specimen at increments of 0.1 mm. At each

point, the transducer would send a pulse of focused energy down through the immersion tank. As the energy interacted with materials of different density, the transducer received the reflected energy. An oscilloscope recorded this reflected energy, displaying received energy amplitude as a function of time and provided a 1-dimensional scan known as an A-scan, as shown in Figure 3.4. As discussed in Chapter II, multiple A-scans are combined into a single 2-dimensional greyscale image known as a C-scan, which displays the maximum amplitude of return energy received by the transducer over its entire path. The MAPPs II system allows manual selection of sample data, called gating, which only compiles returns from a selected time window of the total signal received by the transducer. By gating the A-scans, a C-scan provides the maximum amplitude across a selected depth inside the specimen.

In order to provide calibration and verify accurate scan results, two flat bottom hole (FBH) standards were scanned. By using FBH standards during data collection, the UT transducer gain was calibrated to account for variations in environmental conditions when each scan was collected. These standards consisted of two wrought Ti-6Al-4V right cylinders 76.2 mm in diameter and 50.8 mm tall. Each standard was manufactured with a 25.4 mm deep cylindrical hole, 0.25 mm and 0.50 mm in diameter for the two standards, respectively. These holes were then filled with a matching cylinder of wrought Ti-6Al-4V and provide a repeatable standard for ultrasonic inspection testing.

Ultrasonic scans were conducted on the four specimens through the side scan face, with each of the manufactured voids on the same plane as the transducer's focus. Specimens were then rotated along their X-axis and scans were repeated through the top scan face, now with the manufactured voids out of the focal plane of the transducer. See Figure 3.1(b) for side scan face and top scan face locations. Scans were also accomplished on the two FBH standards before scanning to calibrate the MAPPS

II pulse generator gain. In order to maintain a consistent baseline for each scan, the gain was adjusted until the maximum amplitude of the FBH returns corresponded to 80% of the maximum sensitivity of the transducer. After a batch of scans was completed, the FBH standards were scanned again to verify the equipment remained calibrated throughout the collected scans.

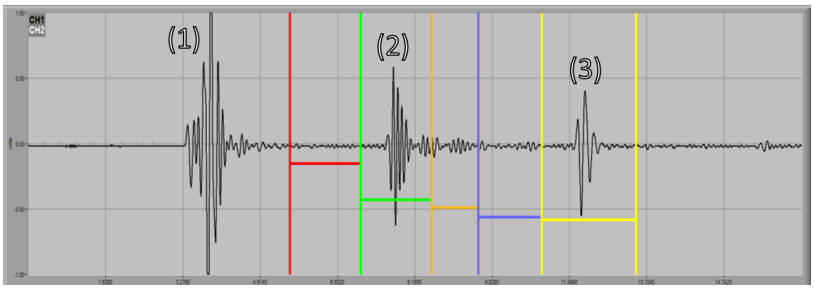

Figure 3.4. PNF A-scan as viewed on MaPPs II Data Acquisition Digital Oscilloscope. In this A-scan, several clear returns are seen, including: (1) the front wall return, (2) a void, and (3) the back wall return. The colored lines represent processing gates viewed through the MaPPs II system during data collection. Each gate isolates a section of the scan return data corresponding to a specific window in time.

After initial testing was completed, an additional set of scans was devised. During data collection through the top scan face with the transducer focal plane out of focus with all known voids, significant background signals were observed. After post-processing, only the two voids nearest the focal plane of the transducer were detected in PNN, and one near-focused void detected in PNF. From these observations, adjusting the focal plane of the transducer was investigated to determine if this change would affect void detection success. Six additional scans were completed on PNN, with the transducer height adjusted so its focal plane matched the Z-axis height of one of the six known voids. These six scans, when combined, doubled the number of voids successfully detected. The full results from these scans are discussed in Chapter IV.

3.5 Data Processing

Raw scan data was read into an array using a Fourier Transform to decompose the signal into its frequencies. Frequencies below 0.5 MHz and above 20 MHz were filtered out. This frequency data was converted into the time domain for each A-scan. Since ultrasonic waves travel at a constant velocity in a homogeneous medium, time corresponds to distance through each sample. The resulting time-domain A-scans are transformed into an array where the maximum value of each A-scan is converted into an 8-bit value. The C-scan is an array of 8-bit values and is visualized by generating a gray scale image where each value in the array linearly corresponds to a pixel ranging between 0 and 255. Zero corresponds to the lowest signal amplitude received and 255 corresponds to the maximum signal amplitude received. An example of a C-scan is shown in Figure 3.5.

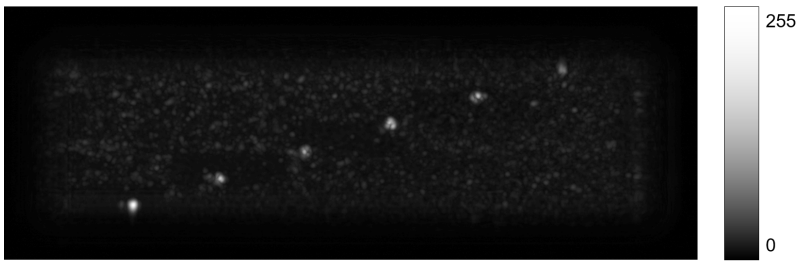

Figure 3.5. RCN side surface through thickness C-scan generated after gating front and back wall returns. Maximum amplitude returns are assigned a pixel value, with higher pixels indicating stronger returns. Six voids are shown in this C-scan, represented by the 6 white dots.

Since a C-scan displays the maximum signal amplitude received, gating is required to isolate scan data. By setting "gates" around an area of interest, an image is generated that ignores previous and future data. This allows the removal of unwanted amplitude spikes such as those from front wall reflections which would dominate any useful data within the specimen. Four gray scale images were generated using two different gating techniques. The first images were built from scans taken through the

side scan face. UT scan return data between the front and back wall returns was isolated for analysis and is referred to as the side surface through-thickness C-scans. The second set of images were built from scans taken through the side scan face, with scan data isolated from immediately before and after the back wall returns and is referred to as the side surface back wall C-scans. The third images were built from scans taken through the top scan face, with scan data isolated between the front and back wall returns. This data is referred to as the top surface through-thickness C-scans. The fourth images were built from scans taken through the top scan face, with scan data isolated from immediately before and after the back wall returns and is referred to as the top surface back wall C-scans. This entire process was completed using an in-house AFRL/RX data processing script.

Once the raw scan data was compiled and converted into gated C-scans, the gray scale images were imported into a processing script for further analysis of scan results. Due to the nature of the C-scan, image processing techniques provide tools to explore the results. Two filtering techniques were used in this analysis, "erosion" and basic intensity filtering. Erosion is a form of morphological image processing using a structuring element to compare an image pixel to neighboring pixels. When eroding an image, the processor selects a structuring element, in this case a circle, to determine neighboring pixels. Using this structural element, each pixel is set to the average pixel value of its neighbors. This process removes the intensity of small spikes due to signal noise while maintaining pertinent image elements [27]. The application of erosion can be seen on a UT C-scan in Figure 3.6, below. A basic intensity filter was the other technique used to remove small spikes in amplitude from images. Using feature detection techniques and thresholding, pixel values below the threshold were set to 0 until only the known intentional voids were detected. This technique also provided a basic value of the background noise for each specimen.

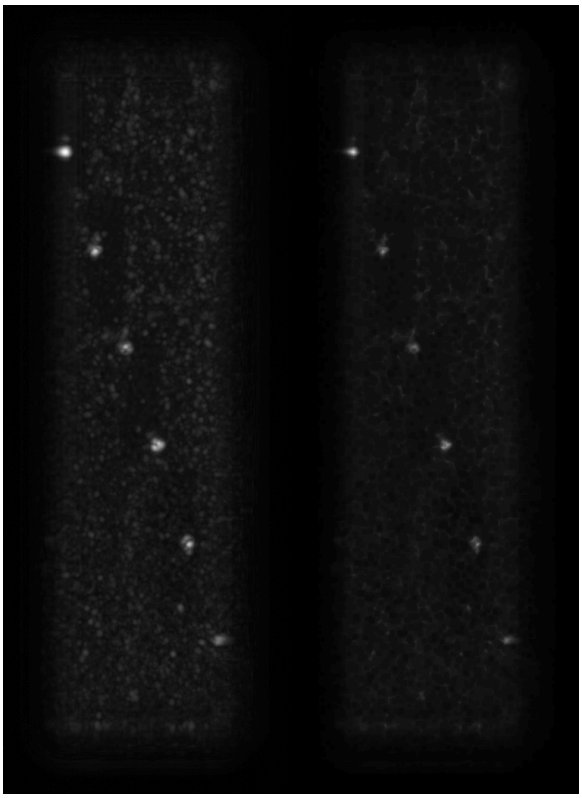

(a) **(b)**

Figure 3.6. Example erosion process performed on UT C-scan of PCN, through the side scan face with through-thickness gating

3.5.1 Circular Hough Transform

Based on successful usage in previous research, the next image processing technique used in this analysis was the Circular Hough Transform [24]. The Hough Transform is a feature extraction technique used to detect circular objects in a digital image.

This process determines an array of pixels with the highest gradient, which are grouped based on a similar distance to an arbitrary center point. The resulting points are set as the circumference of a circle [18]. This process returns points in an image the function believes are circular, with location and radius data. Using a threshold filter, the Hough Transform was repeatedly applied to each through-thickness image until only 6 circles were detected. While the circular Hough Transform does not require prior knowledge of the number of circular objects to look for, the algorithm for the threshold filter required this target number. The lowest pixel intensity was then recorded for comparison to the other samples.

3.5.2 Speeded Up Robust Features

The last image processing technique used was Speeded Up Robust Features (SURF). SURF is a scale invariant processing technique designed to detect unique features in a digital image using local pixel gradients. Utilizing Hessian matrices, SURF identifies points of interest based on vertical and horizontal wavelet responses from integral images in 6-pixel grids [19]. The SURF processing function in MATLAB ® outputs interest point locations, direction, and a strength metric. The 6 strongest points from this output were then isolated and recorded for further analysis. SURF processing was applied to all four C-Scans for each specimen. Once complete, the locations of each SURF point was compared with known void coordinates to determine detection

success. The local maximum image pixel intensity was then calculated using the SURF point coordinates of these successfully detected voids.

3.6 Summary

This chapter presented the procedures followed to collect data to support determination of UT effectiveness on EBM samples of Ti-6Al-4V manufactured with various treatments. Four specimens were selected with identical geometries consisting of rectangular prisms with 6 intentional voids at various depths. These specimens were each manufactured with differing combinations of powder type, contour mode, and melting mode. Each specimen was then ultrasonically inspected using a computer controlled UT system. The results were then processed using MATLAB scripts and greyscale image processing techniques.

IV. Analysis and Results

4.1 Chapter Overview

After completion of the methods described in III, post processed images from ultrasonic scans were compared for detection success. Detection success was determined by proximity of an image feature point to a known void location. Points of interest were initially ignored if they did not correspond to a known void location. Processed images were then compared in order to analyze how UT is affected by the controlled manufacturing process variables. This chapter presents the results of this process along with an analysis of those results.

4.2 Ultrasonic Scan Analysis - System Calibration with Flat Bottom Hole Standards

During UT scan data collection, flat bottom hole standards were utilized in order to provide a relative measure for image processing and to verify the UT equipment did not vary during a scan data set. Collected flat bottom hole standard images were processed in a similar manner to experimental data.

Due to their design, the flat bottom hole standard's analysis presents a method to baseline the use of the SURF strength metric for analysis of the test specimens. The void is considered an ideal shape for detection when using UT methods. Since the SURF strength metric is a non-dimensional measure of the pixel gradient towards an interest point, a stronger strength metric indicates a stronger contrast between an interest point and its surroundings.

Using the SURF Processing technique, the void was easily detected in the #1 flat bottom hole specimen as an image feature with a strength metric of 64914 and maximum pixel intensity of 255, and is shown in Figure 4.1. This is the strongest

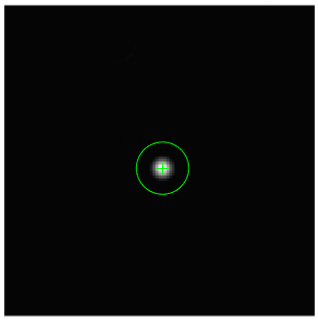

Figure 4.1. #1 Flat Bottom Hole SURF analysis. The standard is manufactured from wrought Ti-6Al-4V and therefore has minimal background noise. This increases the SURF strength and the pixel intensity of the known void.

strength metric and pixel intensity seen using this process and is expected due to the design of the specimen and the resulting contrast presented by the scan.

4.3 Ultrasonic Scan Analysis - Side Scan Face

The first scan data collected was through the side scan face of each of the four test specimens. With the side scan face presented, all six voids in each specimen were coplanar with the focal plane of the UT transducer. The collected data was then processed using the Circular Hough Transform and SURF techniques. Further, when using the SURF technique, scan images were gated around two areas of interest. The first is the through-thickness, with the front and back wall returns removed, and the second with only the back wall return analyzed.

4.3.1 Circular Hough Transform - Side Scan Face

Utilizing Circular Hough Transform and a thresholding intensity filter, the noise in each of the specimens was evaluated. As seen in Figure 4.2, all six voids were detected in PREP/Contour/No Melt (RCN), P841/No Contour/No Melt (PNN) and P841/No Contour/Focus Change (PNF). However, only five voids were successfully detected in PREP/No Contour/No Melt (RNN). Additionally, in PNN and PNF the intensity filter was applied, but thresholding was not required for successful detection of all six voids. Meanwhile, the filter applied to RCN and RNN used thresholded pixel values of 46 and 45, respectively, in order for the Hough Transform to find 6 circular elements.

4.3.2 SURF Processing - Side Scan Face

SURF processing provided an additional void detection technique that required no intensity filtering registered non-circular features. By comparing the strength metric of each of these SURF points, characteristics of each of the specimens were analyzed. As seen in Figure 4.3, SURF processing was able to successfully detect all six voids in RCN, and PNN. Only five voids were detected in RNN and PNF, with the sixth

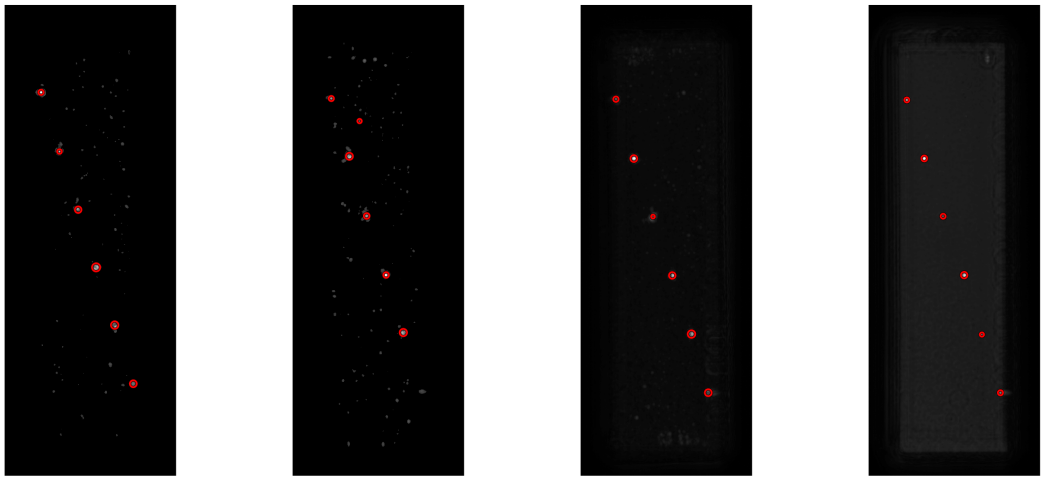

(a) RCN **(b) RNN** **(c) PNN** **(d) PNF**

Figure 4.2. Side surface Through Thickness C-scans after Circular Hough Transform. The red circles correspond with identified circular elements using the Hough Transform function.

SURF point identifying an already detected void in each case. PNF and RNN had the strongest strength metrics with an average of 25353 and 25130, respectively. In addition to strength metric, pixel intensities were also recorded for each successful void detection. Similar to the strength metric, RNN and PNF had the highest average pixel intensity with average values of 205.2 and 171.5, respectively. With all 6 voids at the focal plane of the transducer, strong returns are expected when using ultrasonic scanning. These scans were also produced perpendicular to the build direction, with the ultrasonic waves traveling along the build layers.

Rather than identify strong signal returns from the voids themselves, analysis of the back wall returns attempted to identify any lack of returns due to a shadowing effect of the voids positioned in front of the back wall. SURF processed back wall gated scans were not as successful in detecting voids through the side scan face with 63% less voids detected when compared with the through thickness scans. These scans are shown in Figure 4.4. Voids nearest the edges of each sample were always

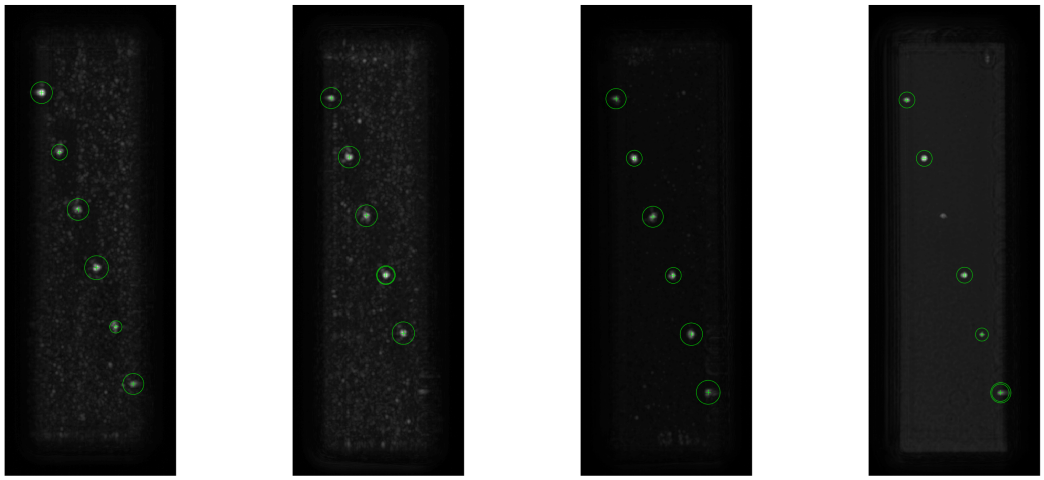

(a) RCN **(b) RNN** **(c) PNN** **(d) PNF**

Figure 4.3. Side surface through thickness C-scans after SURF processing. The green circles identify points of interest identified by the SURF function. Interest points were compared with known void locations to determine void identification success.

undetected using this process due to increased energy scattering near the outside edges of the specimen as the UT wave propagates towards the back wall surface. The most voids, 3 out of 6, were successfully detected in RCN, and only 2 voids were detected in PNN. No voids were successfully detected in RNN and PNF.

The blocks with detected voids from the back wall signals appear to have no unifying factor explaining their detection success when compared with the remaining specimens. Both blocks have different powder and contouring modes, and, while both were manufactured with the no melt strategy, RNN was as well. This leads to two possible explanations: some additional manufacturing, environmental or test condition adversely affected these scans, or an inverse relationship exists between powder selection and contour mode when utilizing the back wall gating method. Based on the results of the through thickness scans, the PREP powder samples may produce too much noise to create clean void shadows in the back wall gate. However, when the contour mode is activated, the more well-defined edges of the voids may increase the

sharpness of the shadows enough to be identified on the back wall. Inversely, while the P841 samples may produce clearer scans, the activation of the "focus change" mode may produce voids that do not reflect enough ultrasonic energy away to produce identifiable gaps in the back wall return scans. In addition to increased void detection success, both blocks also exhibited evidence of the build layer direction in the back wall returns. Table 4.1 summarizes the number of detected voids, SURF strength and local maximum pixel intensity for each test specimen. Overall, analysis of the back wall scans results in fewer correctly identified voids than through-thickness scans. This is a result of the ideal focal plane distance for void detection for through thickness gating, combined with poor detection of near-edge voids on the back wall gating.

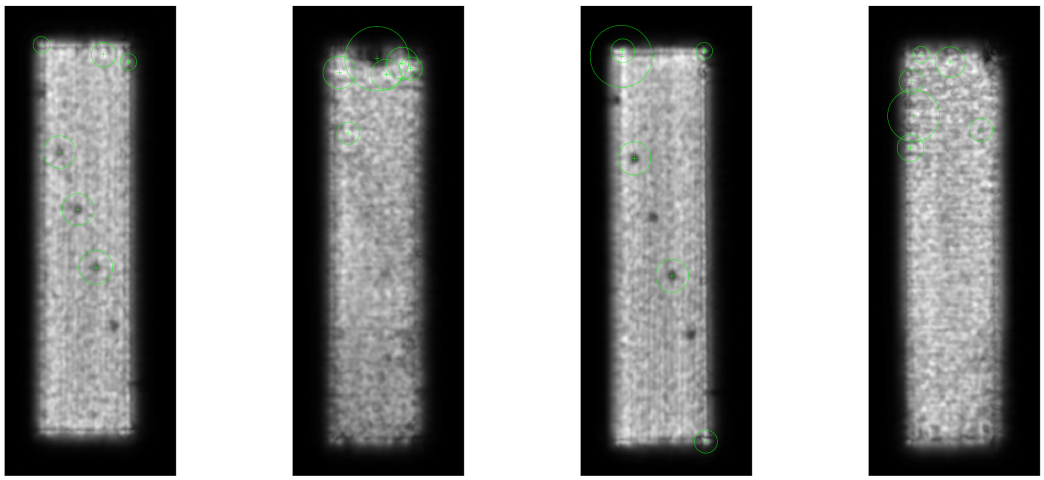

(a) RCN **(b) RNN** **(c) PNN** **(d) PNF**

Figure 4.4. Side surface back wall C-scans after SURF processing. The green circles identify points of interest identified by the SURF function. Interest points were compared with known void locations to determine void identification success. Evidence of the build layer are also seen in the vertical striations of 4.4(a) and 4.4(b).

Table 4.1. SURF Point Data Summary - Side Scan Face

Build	Side Through Thickness			Side Back Wall		
	Voids	Average Strength	Average Pixel Intensity	Voids	Average Strength	Average Pixel Intensity
RCN	6	21163	186.8	4	5681	91.5
RNN	5	28917	205.2	0	X	X
PNN	6	17791	161	3	9890	81
PNF	5	22366	171.5	0	X	X

4.4 Ultrasonic Scan Analysis - Top Scan Face

After the side scan face data was collected, the specimens were rotated to present the top scan face to the UT transducer. Again, after UT scans were completed, the resulting images were processed using the Circular Hough Transform and SURF Process techniques. SURF processed images were analyzed using both gating protocols.

4.4.1 Circular Hough Transform - Top Scan Face

The Circular Hough Transform was unsuccessful at detecting any voids through the top scan face. As seen in Figure 4.5, top scan face images contained significant background noise not removed using the threshold filter previously described. Due to this noise, the Circular Hough Transform could not accurately isolate six image features corresponding to known void locations. This is the first evidence suggesting there are difficulties when UT scanning from this perspective. While the decrease in detection success is potentially due to the voids no longer lying on the focal plane of the transducer, this does not account for the increase in background noise. The increased background noise likely results from the view of the transducer through the specimen, which is now looking parallel with the build direction and through the build layers. This phenomena is investigated in further sections.

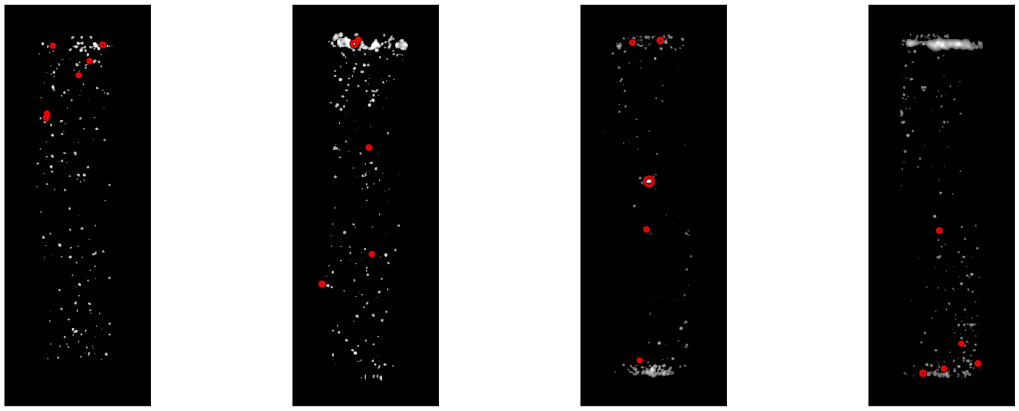

(a) RCN **(b) RNN** **(c) PNN** **(d) PNF**

Figure 4.5. Top surface Through Thickness C-scans after Circular Hough Transform. The red circles correspond with identified circular elements using the Hough Transform function. No known voids were identified from the the background noise using this analysis.

4.4.2 SURF Processing - Top Scan Face

As in the Hough Transform analysis, increased noise made the voids in all four specimens from the top surface through-thickness C-scans more difficult to detect. As seen in Figure 4.6, scanning through the build layers generates additional returns which the image processing techniques used cannot filter out. No voids were identified in RCN and RNN, and only 2 and 1 voids were successfully detected in PNN and PNF, respectively.

Visual analysis of the C-scans shows blocks manufactured with PREP powder have the most return noise, building on evidence seen in Section 4.3.1 suggesting powder plays a role in detected background noise levels. The three voids detected between the P841 Powder specimens were the closest to the focal plane of the transducer. This verifies the assumption void detection probabilities increase when voids are near or on the focal plane of the transducer. Additionally, these results indicate scans through the build layers inhibit return energy more than scans along the build layers. As the

UT wave passes through each layer, energy is dissipated away from the transducer, lowering overall return energy while increasing the prevalence of scattered energy reflected back to the transducer. Combined with off-focal-plane voids, this effect resulted in poor detection success across all four samples.

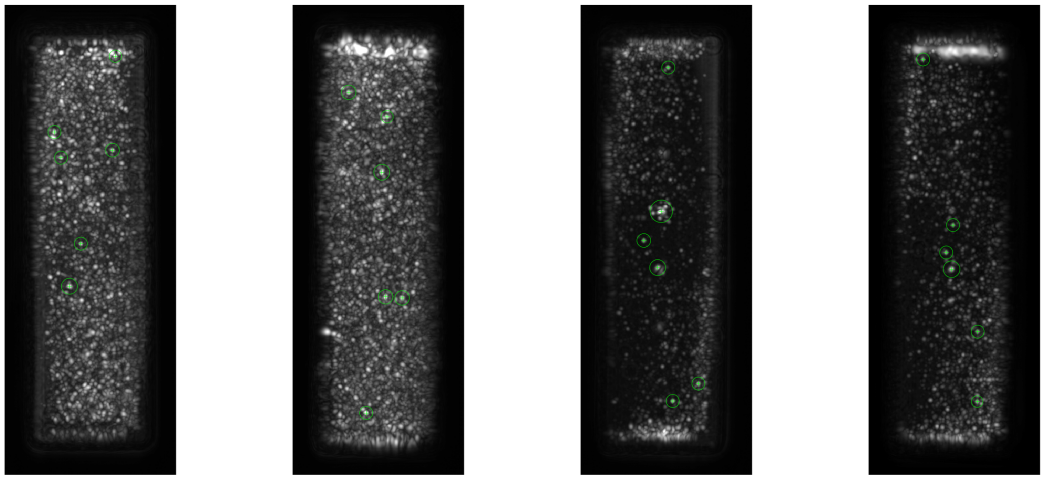

(a) RCN **(b) RNN** **(c) PNN** **(d) PNF**

Figure 4.6. Top surface through-thickness C-scans after SURF processing. The green circles identify points of interest identified by the SURF function. Interest points were compared with known void locations to determine void identification success.

Due to the poor detection rate for the processes shown in 4.6, top scan face C-scans were then gated on solely the back wall returns. SURF analysis of this scan data, shown in Figure 4.7, provided more successful detection as three voids were identified in RCN and PNF, four voids in RNN, and five voids in PNN. Since the contour mode treatment reinforces void edges, scan returns on contoured voids were expected to reflect more energy. However, the voids of the contoured specimen created the least identifiable shadows on the back wall, with the least amount of voids detected by SURF and the lowest average strength of 755. PNN had the strongest back wall shadows, with the 5 identified voids having an average strength of 14250. It is also noted the SURF points generated on the back wall shadows have significantly

weaker strength metrics with values varying between 5% and 50% of the SURF points identifying direct returns. This is due to the reflective nature of these returns. As UT wave energy propagates through a specimen, much of the energy is absorbed or reflected away. This scattering effect softens the edges of the back wall shadows decreasing pixel gradients in the C-scan and therefore decreasing the strength of the SURF points.

Despite this, the back wall scans presented a much more reliable detection technique when compared with the through thickness scans from the top scan face perspective. While less energy is reflected by the voids themselves when passing through build layers, this effect increases the fidelity of back wall returns. Additionally, the diffusion of energy through the build layers increases the apparent size of the voids, increasing the ability of UT to identify voids, while diffusion of energy on background noise destructively interferes and is effectively canceled out. A summary of SURF point and Pixel intensity data for the Top Scan Face is shown in Table 4.2.

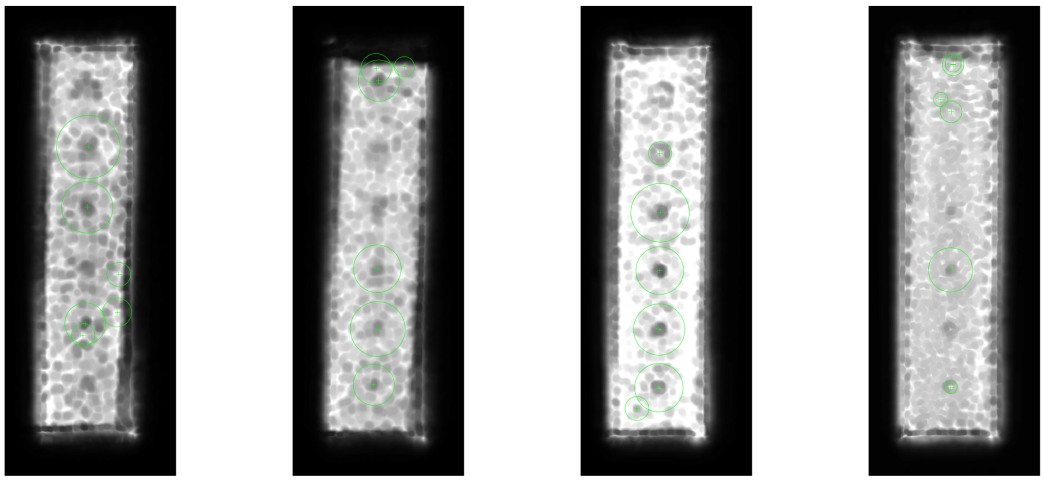

(a) RCN **(b) RNN** **(c) PNN** **(d) PNF**

Figure 4.7. Top surface back wall C-scans after SURF processing. The green circles indicate points of interest identified by the SURF process. Interest points were compared with known void locations to determine void identification success.

Table 4.2. SURF Point Data Summary

Build	Top Through Thickness			Top Back Wall		
	Voids	Average Strength	Average Pixel Intensity	Voids	Average Strength	Average Pixel Intensity
RCN	0	X	X	3	755	106.3
RNN	0	X	X	4	5678	128.3
PNN	2	27416	227.5	5	14250	147
PNF	1	15933	158	3	4781	204

4.5 Ultrasonic Scan Analysis - Top Scan Face with Focal Plane Adjustment

After initial data processing revealed through-thickness scans from the top scan face presented images were difficult to analyze, an additional set of scan data was collected on specimen PNN. The goal of these scans was to determine whether adjusting the focal plane of the transducer would increase the number of voids detected. During these scans, the transducer focal plane was adjusted to match the depth location of each known void location.

While adjustment of the focal plane changed the overall quality of the images, this did not have a significant impact on detection of voids during individual scans, as seen in Figure 4.8. Detection success was still low, with three out of the six scans identifying two voids each, while the remaining three scans only found one void each. Again, only voids near the focal plane were successfully detected using the SURF processing technique. Table 4.3 displays SURF point strength compared to scan focal point depth and void location depth.

While the individual scans with adjusted focus did not increase detection success, an aggregate scan technique would result in all six scans combined together. When combined, four out of the six voids are successfully detected, with three of the voids detected in two or more scans. This redundant detection increases the probability

an indicated void is actually present. However, this technique was still limited, with the 2 and 23 mm deep voids undetected in any of the six scans, despite an adjusted focal plane to their exact depth. This is likely due to their signal returns mixing with front and back wall returns and being gated away, a common issue with UT. With the focal plane adjusted near these points, effects of the front and back wall are shown in Figure 4.8 (a) and (f).

It was also noted adjusting the focal plane to a void's exact depth did not increase the chance of detecting a void at the corresponding depth, with only two of the voids detected when the transducer was focused to the same depth. This indicates, while the focal plane should approximate a void's height to increase its probability of detection, the focal plane does not need to coincide with the void exactly.

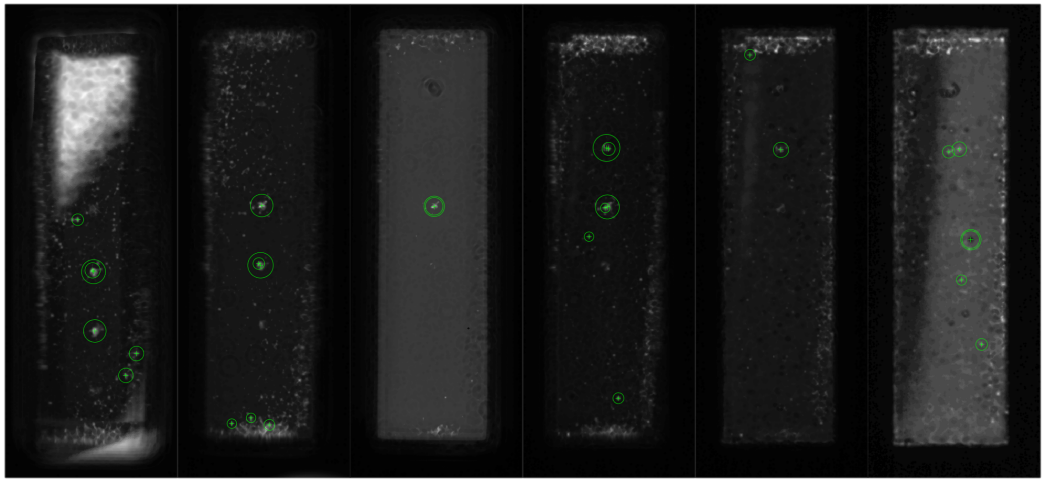

Figure 4.8. Top surface through thickness C-scans after SURF processing of PNN. The focal plane was adjusted to match location depth of each known void. The green circles identify points of interest identified by the SURF function. Interest points were compared with known void locations to determine void identification success.

In addition to through thickness gates, back wall gating was also applied to the six variable focal plane scans collected with PNN, seen in Figure 4.9. Again, no change in the ability to identify voids was observed in individual scans, with each the first scan detecting three of the six voids and the remaining five scans detecting five. This

Table 4.3. SURF Data Points of PNN with Variable Focal Depth, Top Scan Face Through Thickness

		Scan Depth					
		2.0	6.2	10.4	14.6	18.8	23
Void Depth	2.0	x	x	x	x	x	x
	6.2	15059	x	x	x	x	x
	10.4	14343	7027	x	x	x	x
	14.6	x	14172	7747.2	3459.6	x	x
	18.8	x	x	x	6624.9	3000.3	4183.7
	23	x	x	x	x	x	x

matches the success of the original scan with mid-plane focal point. Similar to the through thickness gated images, effects of the front wall are shown in Figure 4.9 (a) when the focal plane of the transducer is adjusted nearby. The effects of focal plane adjustment are also observed in the clarity of the individual voids. The voids nearest the focal plane in each scan appear darker then voids further away, and as seen in Table 4.4, the strength metric of the SURF point increases as well.

When combined together, the six scans successfully detected all six voids, with redundant detections for each void. Among the six scans, as few as two scans combine to detect all six voids. Based on this high success rate, optimization of a back wall scan method with two or three scans at varying depths is possible to confidently detect any unknown voids. Combining the increases in detection success from the through-thickness variable focus scans and the single focus back wall scan, this method presents a viable alternative when attempting to detect voids through the build layers of an AM component.

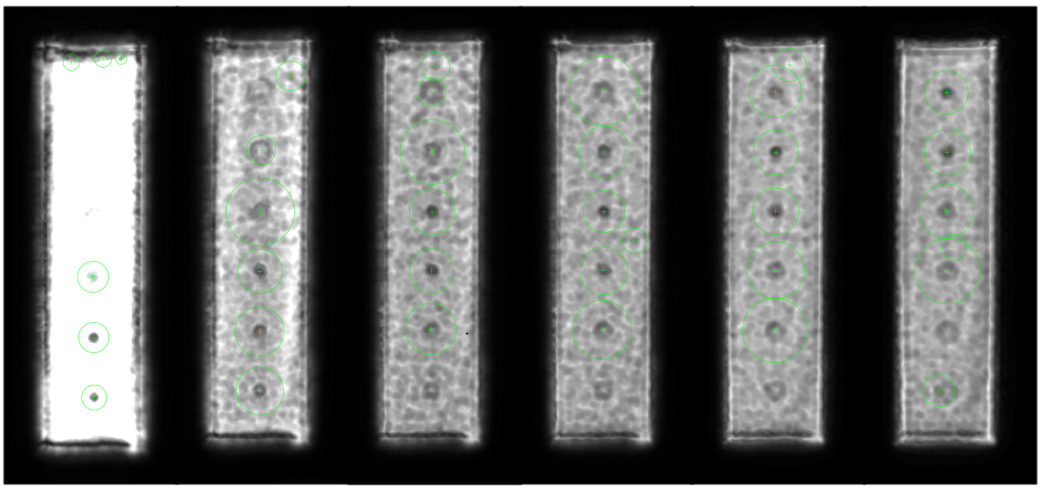

Figure 4.9. Top surface back wall C-scans after SURF processing of PNN. The focal plane was adjusted to match location depth of each known void. The green circles identify points of interest identified by the SURF function. Interest points were compared with known void locations to determine void identification success.

Table 4.4. SURF Data Points of PNN with Variable Focal Depth, Top Scan Face, Back Wall

		Scan Depth (mm)					
		2.0	6.2	10.4	14.6	18.8	23
Void Depth (mm)	2.0	2986	5865.9	x	x	x	2794
	6.2	3678.3	6852.7	4586	4346	3764	x
	10.4	385.6	8520.6	11231	8002	4741	3191
	14.6	x	4886.6	11268	12251	11587	4661
	18.8	x	4627.4	4800	8009	12353	10157
	23	x	x	3611	4489	6034	9313

4.6 Analysis of Results

This research attempted to determine the effect of several EBM manufacturing variables on the ultrasonic inspection of geometrically identical Ti-6Al-4V specimens. The data collected provided images through the production of UT C-Scans and quantitative values through the use of threshold filter values, SURF point strength metrics, image pixel values and detected image feature locations. Specimen orientation had the greatest impact on all scans, with clearer images produced by scanning along the

build layers versus through the build layers. This is due to increased signal observed perpendicular to the build layers, likely due to distributed porosity or flat microstructures that lie parallel with the build layers. The effects of these signals was mitigated by adjustment of the transducer focal plane and adopting back wall gating methods.

4.6.1 General Trend Analysis

Before any digital image processing was accomplished, the images were visually analyzed to determine if any immediate trends were apparent. In both the side scan, through thickness and top scan, through thickness scans, a clear change was observed in the background returns from the PREP powder specimens to the P841 specimens, indicating powder type may effect background noise returns both through the build layers and along the build layers. A change was also observed when comparing the back wall gated scans through both scan surfaces. RCN and PNN both produced clearer and brighter C-scans than RNN and PNF, with more well defined void edges. While these scans don't directly correspond with any individual scan effect, they may indicate an inverse relationship between variables when analyzing back wall returns, with PREP powder specimens producing clearer scans with contour mode activated while P841 powder specimens produce noisier scans with focus change activated. This is likely due to the contour mode increasing the clarity of voids while focus change reduces clarity. When combined with the clarity of P841 and noise of PREP samples, RCN and PNN produce the clearest back wall returns.

The side scan face, through thickness C-scans also revealed an interesting phenomena in the PREP powder specimens. Amongst the background noise returns, a distinct "stair stepping" shadow is seen in Figure 4.10. After analysis, it was determined these shadows line up with stair step and inverse stair step test specimens manufactured on the same build plate as the specimens used in this research. This

alignment presents strong evidence the two stair step test specimens influenced the fabrication of the RCN and RNN blocks sufficiently to induce a change in their structure detectable by UT. It is hypothesized that the EBM machine was not set up to handle the sudden change in line length when each step occurred. This led to an immediate change in the melted characteristics of the powder in these two specimens detected by the ultrasonic wave.

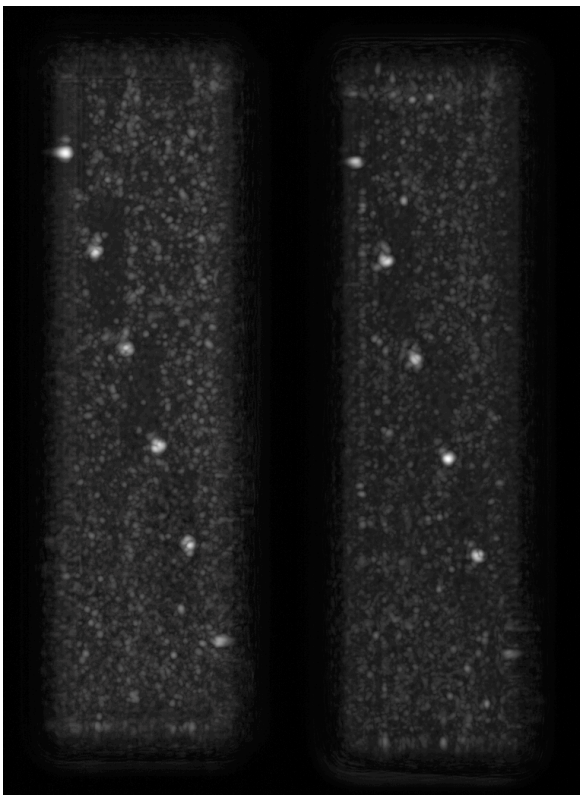

(a) RCN **(b) RNN**

Figure 4.10. Stair step shadows seen in PREP powder specimens.

Previous research on EBM samples of Ti-6Al-4V indicated that automated detection of voids using the circular Hough transform was possible [24]. Using similar source powder to P841, a 10 MHz transducer and with all voids aligned with the transducer focal plane, the circular Hough transform was able to detect voids as small as 0.51 mm in diameter, with zero voids undetected [24]. A similar application

of the transform was used for this research with comparable results under similar conditions. Processing of the PNN and PNF specimens yielded 100% detection of voids in C-scans through the side scan face, and with all voids in line with the focal plane of the transducer. When switching to a different powder, RCN and RNN had slightly lower detection success with one void in RNN undetected by the transform. Moving the voids away from the transducer focal plane, C-scans through the top scan face did not yield any detected voids by the transform.

While the circular Hough transform provided limited insight, the threshold filter used during initial processing provided a quantitative value to compare the Side Scan, Through Thickness images. While the PREP powder specimens detected voids after application of a threshold filter of 46, the P841 specimens required no thresholding to detect the six known voids. This corresponds to the initial qualitative impressions of the background image quality when comparing the PREP and P841 powder samples.

When comparing successful detection rates among SURF points, several trends are observed. The Top Scan, Through Thickness scans again indicate a 50% increase in detected voids between the PREP and P841 powder specimens, with all detected voids limited to the P841 specimens. Also, the Side Scan, Back Wall scans corresponded with the initial visual assessment of these images. In addition to detection of voids, the SURF process also provided a strength metric for each point. Since the strength metric indicates a stronger pixel gradient, the strength metric the intensity of a voids reflected energy relative to the dispersed energy. Lastly, a maximum local pixel intensity was calculated for each SURF point identified, correlating to the local reflected energy.

Overall, average strength correlated slightly with powder type, with P841 producing stronger points, again supporting conclusions from other assessments. Interestingly, pixel intensity increased with the PREP powder samples, indicating additional

noise is due to increased signal reflectivity of PREP versus P841 powder. Increased strength was also correlated with no melt mode versus focus change mode. This coincides with the estimation that the voids in the focus change specimen are partially adhered and do not create an adverse change in density to reflect as much UT energy as voids filled with unmelted powder. No significant correlation was found based on pixel intensities.

Additionally, increased strength was correlated with contour mode deactivated across all scans. While it was expected that the activation of contour mode would create more defined, and therefore stronger, void structures, this result indicates the opposite. Since the contour mode creates more defined internal structures, it is hypothesized that the contoured voids in RCN are closer to the design size. The edges of non-contoured voids may potentially transition more slowly from solid material to unmelted powder, resulting in a physically larger void. This indicates designers of future test specimens must take care when sizing voids if contour mode is deactivated. However, contour mode did correlate with an increase in pixel intensity, and is possibly due to the observed reflectivity of PREP over P841.

4.6.2 Statistical Analysis

While the general trend discussed in the previous section may provide insight to the production of voids used in NDI test specimens, it is important to statistically study this information. Since this research is focused on the differences in detection success with different manufacturing treatments, a t-test was devised to determine if there was a statistical difference in the strength of the image features detected under each treatment category.

Due to the limited successfully detected points in both the Side Scan, Back Wall and Top Scan, Through Thickness results, points used in this analysis were limited to

those detected in the Side Scan Face, Through Thickness and Top Scan Face, Back Wall returns. For each treatment category, the SURF point strength metric for each detected void was partitioned into one of the two treatments types in that category. The means of these two groups were then compared using a student t distribution, with the null hypothesis that the differences in the means are equal to zero. A 90% confidence interval was set for these tests and p-values less than 0.10 would reject the null hypothesis. Across all three categories, the p-value calculated from each t-test performed indicated rejection of the null hypothesis is not possible, meaning there is not enough information to say there is a difference in the strength for each category. The data was also further grouped into each scan perspective, resulting in similar conclusions. The tabulated p-values for each of these t-tests are shown in Table 4.5.

SURF strengths based on scan perspective were also tested with this method, grouping the strength from each successful void detection into side scan face or top scan face categories. The p-value of 0.0017 is well within the confidence interval previously defined and supports the rejection of the null hypothesis, indicating that there is a difference in strength metrics when the scan perspective relative to the build layer is changed.

Table 4.5. P-values from SURF strength-treatment differences t-test

	Contour Mode	Melting Mode	Powder	Scan Direction
Combined	0.37	0.96	0.94	0.0017
Side Scan, Through Thickness	0.79	0.97	0.43	X
Top Scan, Back Wall	0.72	0.22	0.19	X

While mathematical comparison of these p-values is not possible, they can provide further insight into the trends discussed in the previous section. With significantly high p-values in both perspectives, Contour Mode appears to have the least effect on the strength metric of detected voids. The melting mode did not have significant

impact on the strength when viewed through the side scan face, however, when the top scan face was gated on the back wall, melting mode appears to have a stronger impact. Lastly, powder is shown to potentially have the strongest impact on detection probability with the lowest p-values observed in either perspective. This agrees with the initial qualitative assessment of the C-scans with the PREP powder specimens having distinct changes in the background returns when compared to the P841 powder specimens.

Detection success results were also statistically compared with similar findings. For these studies, the number of detected voids was subtracted from the number of expected voids for each scan of a specimen. Again, like characteristics were combined in a student-t test with the null hypothesis that the differences in means are equal to zero. The results from these tests are shown in Table 4.6. Powder, contour mode and melting mode all fell short of the 0.10 p-value, implying the null hypothesis cannot be rejected. Scan direction and gating, however, strongly rejected the null hypothesis, supporting the conclusion that scan perspective relative to the build direction plays a significant role in detection success.

Table 4.6. P-values from detection success-treatment t-test

	Contour Mode	Melting Mode	Powder	Scan Direction, Through Thickness	Scan Direction, Back Wall
P-value	0.37	0.38	0.25	0.000073	0.072

4.6.3 False Positive Analysis

In addition to detecting known voids in sample specimens, the SURF processing technique also identified a number of image features of unknown origin. These points may fall into two categories: unknown void structures within the specimen, or false positives identified by the SURF technique. As shown in previous research [17], false positives is a significant issue when attempting to use computer automation to detect

and identify voids in UT scans. These false positives may result from actual changes in the structure of the specimen, or additional noise that was not successfully filtered out by the UT equipment. While these points were initially treated as false positives during the analysis discussed in previous sections, these points are not completely ignored due to the real potential of unknown void generation in AM. The destructive inspection of the test specimens would conclude either possibility. However, with 68 features detected across all 28 C-scans produced, it was determined destructive inspection was impractical.

Since each known void in each specimen was detected from several different perspectives, it is fair to assume that the probability of detection of unknown void structures would increase across multiple scans. To determine which points, if any, were actual voids, a matrix was developed that would compare detected image feature coordinates with other nearby features. For a specific specimen and perspective combination, the distance between each unknown point to every other unknown point was calculated and compared with the calculated variation in SURF point coordinates for the known voids in that specimen.

Across all 68 unknown points, only two points fell within the known point variation. In the back wall gated, PNN variable focus scans, a point was identified in the scan with a focal depth of 2 mm that fell within 13 pixels of a point in the scan with a focal depth of 18.8 mm, seen in Figure 4.11. When analyzed qualitatively, however, it is seen that the SURF points are identifying very different image features. The point in Figure 4.11a is detecting an edge in the primary return signal from the specimen back wall, while Figure 4.11b identifies a small variation in the back wall return in a similar location. Overall, no potential false positive points identified during this research were verified as unintentional voids using this approach. Due to these results, it was determined no destructive inspection was necessary on any unknown points.

It is important to note the unverified signal data may still result from reflections off of actual defects within the specimens. The technique discussed in this section assumes repeatable detection of defects from multiple perspectives. However, this may not be the case due to defect size and directionality. Due to the 10 MHz transponder used, reliable detection of voids was limited to features greater than 0.61 mm. Natural porosity or microstructures within the specimens would likely be much smaller than this threshold. These smaller features may still produce reflections, but not repeatably for every scan. Additionally, naturally occurring defects typically are aligned with the build layer where they are generated, and therefore may only appear when scanned through the build layers. Ultimately, additional, undetected, voids may still exist in the tested specimens and direct observation through destructive inspection is required to verify their existence.

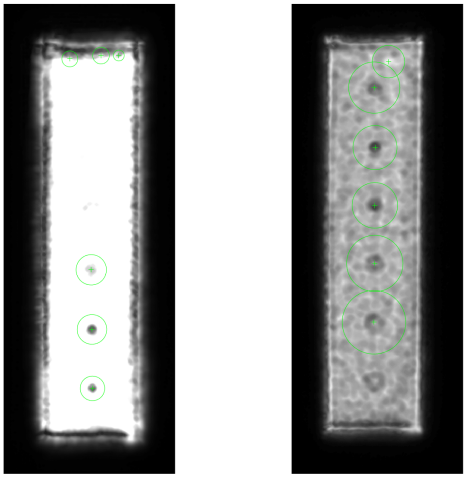

(a) **(b)**

Figure 4.11. Identified images with unknown SURF points in relative proximity.

V. Conclusions and Recommendations

5.1 Review of Research Objectives

The primary goal of this research was to assess the effect of various manufacturing treatments on the response of UT when used to detect known voids in EBM Ti-6Al-4V. To assess these manufacturing treatments this research focused on the following objectives:

1. Determine the influence of different source powders, contour and melting modes on UT results.

2. Determine the influence of varying distances from transducer focal plane on UT results.

3. Determine the influence of build direction relative to scan direction on UT results.

To reach these objectives, UT data was collected from four samples in two configurations. This data was then analyzed using two different types of image processing techniques. Gating was also used to further analyze and assess differences in the tested specimens.

The first objective was satisfied through the use of UT through the side scan face and top scan face with an inspection frequency of 10 MHz. Test results demonstrated no link between manufacturing treatments and UT effectiveness with slight but statistically insignificant trends observed between contour vs non-contour treated voids and "no melt" vs "focus change" treated voids. Additionally, some changes were also observed between the PREP and Arcam P841 powder specimens, with a marked increase in background noise seen in the PREP powder samples, however these factors did not impact void detection.

The second objective was similarly satisfied through the use of UT, however only top scan face data was utilized. Test results indicated that focal plane changes have an effect on void detection success with voids further from the transducer focal plane have a much lower probability of detection. This was seen both in scans where the focal plane was set at the mid-plane of the specimens as well as when the focal plane was adjusted throughout the depth of the specimen. Additionally, another inspection technique was investigated, which analyzed UT signal returns from the back wall of a specimen rather than from the voids themselves. This method was especially effective at detecting voids far from the focal plane of the transducer.

The third objective was satisfied by analyzing results from the side and top scan faces. While scanning along the build layers enabled successful detection of 92% of voids, scans through the build layers resulted in only 12.5% of voids detected. Additional techniques were investigated to improve void detection successes when scanning through the top face, including: back wall gating and adjustable focal depths. By gating C-scans on only the back wall, the effects of voids could be detected by searching for gaps in UT energy. Additionally, scans taken at varying focal depths allowed detection of 66% of voids when gated through the entire thickness of the specimen and 100% of voids when gated on the back wall.

5.2 Discussion of Results

The data collected during this research provided insight into the effect of several manufacturing process variables on UT's ability to detect manufactured voids in EBM Ti-6Al-4V. Analysis shows void manufacture treatment potentially plays a role in the success of UT to detect voids. More data collection is required to increase statistical confidence and support any conclusions made. While all six voids were detected in all four specimens, detection success varied heavily depending on scan perspective.

While the vast majority of UT research relies on subjective analysis of scan images, this research attempted to utilize build on prior research and use greyscale image processing techniques to analyze collected UT data. While the circular Hough transform was shown capable of detecting voids within the transducer focal plane in optimized powder [24], the adaptation of this technique to other perspectives was not as successful. Overall, Circular Hough Transforms and threshold filtering of side surface c-scans indicated powder type plays a significant role in void detection and identification success but the application of this technique is limited since natural vacancies rarely present as spheres.

SURF provided a more robust, yet unproven, detection method, with the majority of voids detected from the side surface and top surface back wall scans. While SURF successfully indicated voids in alternate perspectives, this novel technique for void identification requires further analysis to verify its validity. Top surface through-thickness c-scans produced significant background noise which limited detection success. The only voids detected using SURF analysis on these scans were near the focal plane of the transducer, indicating successful detection of voids through the entire thickness would require several additional scans with the focal plane positioned at varying heights. This was further confirmed through the production of six scans at varying focal depths on PNN. While adjusting focal depth did not increase the probability of detection in individual scans, the six scans combined doubled the probability of detection.

Scan perspective played the biggest role in detection success with scans perpendicular to the build layers successfully detected 91.7% of the voids, compared to only 37.5% of voids found in scans parallel to the build layers. New techniques were developed to overcome this issue and through the use of multiple scans at varrying

focal depths and gating on the back wall, detection success parallel to the build layer increased to 100% in PNN.

Powder selection was correlated to some changes in detection parameters including an increase in SURF strength in P841 and an increase in pixel intensity in PREP. An increase in pixel intensity indicates specimens fabricated from PREP powder is more reflective of UT energy than P841, which supports the stronger background noise observed in PREP samples. This increase in background noise inversely decreases the SURF strength of successfully detected voids. Increased SURF strength also correlated with no melt mode versus focus change mode. Voids in the focus change specimen are partially adhered due to some unfocused energy applied to the powder during fabrication. This creates a lower change in density that would reflect less UT energy than voids filled with unmelted powder.

Lastly, decreased SURF strength and increased pixel intensity was correlated with contour mode activated. Since the contour mode applies additional melting energy to the edges of voids, this analysis indicates UT energy is dissipated by the stronger void edges rather than reflected back to the transducer. Additionally, since contour mode strengthens the surfaces of internal design structures, contoured voids are likely closer to their designed size. The increased pixel intensity seen with the contour sample is due to the increased reflectivity associated with P841 with the stronger local reflections from the contoured edges. In other words, the contoured voids initially reflect more energy, but the energy reflection slowly dissipates away from the center of the void, leading to decreased SURF strength. This conclusion increases the confidence of UT in the detection of flaws in a production component, since any unintentional flaws will not receive additional treatment similar to the contour mode.

In order to qualify NDI techniques for AM part verification, accurate natural defect replication through intentional void construction in test parts is required. This

research shows that UT scan data has varying success depending on void manufacturing treatments and researchers must take care when determining the manufacturing route when fabricating voids for UT analysis. These results determined some of the limitations of UT as an NDI technique when analyzing AM parts, especially if applied to voids of unknown depth and location. Application of these techniques become more problematic as more complicated part geometry and void shapes are introduced. Further research is required to refine and perfect the techniques discussed in this paper before their application to production representative components.

5.3 Recommendations for Future Work

The data collected and analyzed in this research provides an initial evaluation of the internal changes observed with UT when AM Ti-6Al-4V components with various manufacturing treatments. This data should provide valuable insight to future AM research, especially when applied to the use of post manufacturing inspection of AM components for aerospace use. However, the data collected during this work is preliminary and many areas were identified for further research.

While the geometry of the tested samples was more complex than used in similar, previous research, the specimens used were still far simpler than production representative components manufactured for an aerospace application [24]. Both sample and flaw geometry were identified as potential areas for future work. Complex flaw geometries that more closely represent naturally generated flaws may create unique hurdles for UT inspection methods that were not identified by inspecting simple spherical voids. Additionally, complex flaw geometry might present challenges to image processing algorithms used when processing and analyzing test samples. Additionally, while the flat sided geometry of the current test specimens are easy to analyze with UT, they are not representative of the complex geometries seen in aerospace applica-

tions, nor does it exercise the full capability of AM. Increased complexity in external geometry of test specimens would provide increased insight into how UT is affected by production representative AM components due to variable changes in reflection energy, surface finish, and wave time of flight (TOF).

Focal plane adjustment and scan techniques were also identified as a significant area for future research. While scans through the top face with a single focal plane were limited in detecting voids, multiple scans with different focal planes were much more successful. Optimizing scanning order and focal depth based on part geometry can lead to increasing the overall probability of void detection while limited the time required for the NDI of a component. Combining focal plane adjustment with back wall return analysis would further increase the potential of these techniques. Further, applying an optimized scan protocol to a blind analysis of specimens with manufactured voids would further verify the potential of this technique.

Throughout the analysis of collected data, detection success was most limited on voids near the edges of the specimen. While UT is regarded as strongest NDI method for deep structure detection, surface or near surface detection is difficult. Future work on investigating and improving detection of near edge voids using UT or supplementing with other volumentric inspection methods, such as radiography or x-ray computed tomography, is warranted.

Appendix A. Detection Success Data

Void	Depth	Powder	Contour	Defect Mode	Void Detection			
					Hough Transform	SURF		
					Side Surface	Side Surface	Top Surface Through Thickness	Top Surface Back Wall
1	2	PREP	Y	No Melt	Y	Y	N	N
2	6.2	PREP	Y	No Melt	Y	Y	N	Y
3	10.4	PREP	Y	No Melt	Y	Y	N	Y
4	14.6	PREP	Y	No Melt	Y	Y	N	N
5	18.8	PREP	Y	No Melt	Y	Y	N	Y
6	23	PREP	Y	No Melt	Y	Y	N	N

Table A.1. P1-3 Detection Success Data

Void	Depth	Powder	Contour	Defect Mode	Void Detection			
					Hough Transform	SURF		
					Side Surface	Side Surface	Top Surface Through Thickness	Top Surface Back Wall
1	2	PREP	N	No Melt	Y	Y	N	Y
2	6.2	PREP	N	No Melt	Y	Y	N	N
3	10.4	PREP	N	No Melt	Y	Y	N	N
4	14.6	PREP	N	No Melt	Y	Y	N	Y
5	18.8	PREP	N	No Melt	Y	Y	N	Y
6	23	PREP	N	No Melt	N	N	N	N

Table A.2. Q1-3 Detection Success Data

Void	Depth	Powder	Contour	Defect Mode	Void Detection			
					Hough Transform	SURF		
					Side Surface	Side Surface	Top Surface Through Thickness	Top Surface Back Wall
1	2	P841	N	No Melt	Y	Y	N	N
2	6.2	P841	N	No Melt	Y	Y	N	Y
3	10.4	P841	N	No Melt	Y	Y	Y	Y
4	14.6	P841	N	No Melt	Y	Y	Y	Y
5	18.8	P841	N	No Melt	Y	Y	N	Y
6	23	P841	N	No Melt	Y	Y	N	Y

Table A.3. S1-3 Detection Success Data

Void	Depth	Powder	Contour	Defect Mode	Void Detection			
					Hough Transform	SURF		
					Side Surface	Side Surface	Top Surface Through Thickness	Top Surface Back Wall
1	2	P841	N	Focus Change	Y	Y	N	Y
2	6.2	P841	N	Focus Change	Y	Y	N	N
3	10.4	P841	N	Focus Change	Y	N	Y	N
4	14.6	P841	N	Focus Change	Y	Y	Y	Y
5	18.8	P841	N	Focus Change	Y	Y	N	N
6	23	P841	N	Focus Change	Y	Y	N	Y

Table A.4. V1-3 Detection Success Data

Appendix B. SURF Strength Metric Tables

P1-3		Q1-3		S1-3		V1-3	
Strength	Void Detected	Strength	Void Detected	Strength	Void Detected	Strength	Void Detected
48190	Y	47852	Y	43492	Y	53819	Y
24054	Y	44689	Y	24735	Y	33611	Y
20723	Y	24189	Y	16134	Y	22503	Y
15376	Y	21570	Y	11934	Y	9159	Y
10500	Y	19125	Y	5697	Y	7672	Y
8132	Y	16076	Y	4752	Y	7434	Y

Table B.1. SURF Point Strengths, Side Scan Face-Through Thickness

P1-3		Q1-3		S1-3		V1-3	
Strength	Void Detected	Strength	Void Detected	Strength	Void Detected	Strength	Void Detected
6906.1	Y	7451.5	N	16331	N	59704	N
6676.6	Y	4564.5	N	11251	Y	57654	N
6141.4	Y	4468.3	N	10291	N	53698	N
5846.2	N	4415.3	N	9241	Y	52111	N
3000	Y	4124.8	N	9079	Y	43040	N
4719.1	N	3494.3	N	8945	N	42657	N

Table B.2. SURF Point Strengths, Side Scan Face-Back Wall

P1-3		Q1-3		S1-3		V1-3	
Strength	Void Detected	Strength	Void Detected	Strength	Void Detected	Strength	Void Detected
36825	N	42656	N	30889	N	32734	N
31403	N	36232	N	30627	Y	21313	N
30355	N	33865	N	24205	Y	17450	N
30230	N	32293	N	19977	N	16405	N
29932	N	29565	N	18786	N	16968	N
29663	N	28325	N	18126	N	15933	Y

Table B.3. SURF Point Strengths, Top Scan Face-Through Thickness

P1-3		Q1-3		S1-3		V1-3	
Strength	Void Detected	Strength	Void Detected	Strength	Void Detected	Strength	Void Detected
10268	N	9817.4	Y	25864	Y	7559.7	Y
8228	N	9130.2	N	15752	Y	3646.4	N
8165	Y	5150.9	Y	13793	Y	3645.3	Y
7917	N	4192.9	Y	10478	Y	3411.9	N
7581	Y	3604.8	N	5361	Y	3378.8	N
6918	Y	3552.4	Y	5336	N	3138.2	Y

Table B.4. SURF Point Strengths, Top Scan Face-Back Wall

Appendix C. SURF Points, S1-3 with Variable Scan Focus Depth

2 mm		6.2 mm		10.4 mm		14.6 mm		18.8 mm		23 mm	
Strength	Void Detected	Strength	Void Detected	Strength	Void Detected	Strength	Void Detected	Strength	Void Detected	Strength	Void Detected
15059	Y	14172	Y	7747.2	Y	6763.3	N	3000.3	Y	4183.7	Y
14343	Y	7027	Y	6033.3	N	6624.9	Y	1125.7	N	3121.3	N
12376	N	5805	N	N/A	N/A	5678.3	N	N/A	N/A	2478.8	N
7707	N	6055	N	N/A	N/A	3459.6	Y	N/A	N/A	1905	N
4694	N	5452	N	N/A	N/A	2489.6	N	N/A	N/A	1781.9	N
4394	N	4554	N	N/A	N/A	2010.5	N	N/A	N/A	1732.8	N

Table C.1. SURF Point Strengths, S1-3 with variable focal depth, Top Scan Face-Through Thickness

2 mm		6.2 mm		10.4 mm		14.6 mm		18.8 mm		23 mm	
Strength	Void Detected	Strength	Void Detected	Strength	Void Detected	Strength	Void Detected	Strength	Void Detected	Strength	Void Detected
3678.3	Y	8520.6	Y	11268	Y	12251	Y	12353	Y	10157	Y
2986	Y	6852.7	Y	11231	Y	8009	Y	11587	Y	9313	Y
385.6	Y	5865.9	Y	4800	Y	8002	Y	6034	Y	4661	Y
313.7	N	5027.9	N	4586	Y	4489	Y	4741	Y	3191	Y
225.8	N	4886.6	Y	3751	N	4346	Y	4277	N	2794	Y
152.9	N	4627.4	Y	3611	Y	3961	N	3764	Y	2594	N

Table C.2. SURF Point Strengths, S1-3 with variable focal depth, Top Scan Face-Back Wall

Bibliography

[1] S. L. Ford, "Additive Manufacturing Technology: Potential Implications for U.S. Manufacturing Competitiveness," Sept 2014.

[2] C. Thomas, "Rapid Prototyping of Large Scale Aerospace Structures," *IEEE Aerospace Applications Conference*, 1996.

[3] M. C. L. Nannan Guo, "Additive Manufacturing: Technology, Applications and Research Needs," *Frontiers of Mechanical Engineering*, 2013.

[4] N. A. Connor McNulty and T. Campbell, "Toward the Printed World: Additive Manufacturing and Implications for National Security," *Defense Horizons*.

[5] Energetics Incorporated, "Measurement Science Roadmap for Metal-based Additive Manufacturing."

[6] K. H. Jess Waller, Bradford Parker and J. Walker, "Nondestructive Evaluation of Additive Manufacturing."

[7] I. Gibson *et al.*, *Additive Manufacturing Technologies*. New York: Springer, 2010.

[8] J. Ruan *et al.*, "A Review of Layer Based Manufacturing Processes for Metals."

[9] A. Sadfar, "A study on Electron Beam Melted Ti-6Al-4V," Ph.D. dissertation, Lund University, 2012.

[10] S. P. Xibing Gong, Bo Cheng and K. Chou, "Powder-Bed Electron-Beam-Melting Additive Manufacturing: Powder Characterization, Process Simulation and Metrology," 2013.

[11] Department of Defense, *Metallic Materials and Elements for Aerospace Vehicle Structures, MIL-HDBK-5J.* Wright-Patterson: Department of Defense, 2003.

[12] ASTM International, *Standard Specification for Additive Manufacturing Titanium-6 Aluminum-4 Vanadium with Powder Bed Fusion*, ser. F2924–14, West Conshohocken, PA.

[13] J. W. Lincoln, "Managing the Aging Aircraft Problem," *Life Management Techniques for Ageing Air Vehicles*, 2001.

[14] AFLCMC/EZGTP, *NONDESTRUCTIVE INSPECTION METHODS, BASIC THEORY, T.O. 33B-1-1*, Robins Air Force Base: United States Air Force, 2014.

[15] S. Tammas-Williams *et al.*, "XCT analysis of the influence of melt strategies on defect population in Ti-6Al-4V components manufactured by Selected Electron Beam Melting," *Materials Characterization*, vol. 102, pp. 47–61, 2014.

[16] Department of Defense, *Military Handbook Ultrasonic Testing Mil-Hdbk-728/6*, Department of Defense, 1985.

[17] J. Baan and A. Volker, "Image Processing Techniques for Ultrasonic Inspection," *17th World Conference on Nondestructive Testing*, 2008.

[18] H. Rhody, "Hough Circle Transform," *Rochester Institute of Technology*, 2005.

[19] H. Bay *et al.*, "SURF:Speeded Up Robust Features," *Elsevier*, 2008.

[20] L. S. Mohammed Albakri *et al.*, "Non-Destructive Evaluation of Additively Manufactured Parts via Impedance-Based Monitoring," Virginia Tech, 2013.

[21] H. Rieder, "On- and Offline Characterization of Components Built by SLM Additive Manufacturing," *AIP Conference*, 2016.

[22] D. Levesque, "Inspection of Additive Manufactured Parts Using Laser Ultrasonics," *AIP Conference*, 2016.

[23] S. Everton, "Identification of Sub-Surface Defects in Parts Produced by Additive Manufacturing, Using Laser Generated Ultrasound," *Additive Manufacturing and 3D Printing Research Group, University of Nottingham*, 2016.

[24] Evan Hanks, David Liu, Anthony Palazatto, "Surface Roughness of Electron Beam Melting Ti-6Al-4V Effect on Ultrasonic Testing," *57th AIAA/ASCE/AHS/ASC Structures, Structural Dynamics, and Materials Conference*, 2016.

[25] Andrew Durkee, Andrew Lingenfelter, David Liu, "Ultrasonic Testing of Manufactured Voids in Electron Beam Melted Ti-6Al-4V," *59th AIAA/ASCE/AHS/ASC Structures, Structural Dynamics, and Materials Conference*, 2018.

[26] E. Schwalbach, "NDE prototypes," AFRL/RX Presentation, March 2017.

[27] Mathworks, "Matlab documentation: Erode image," Mathworks, 2017.